The final publication is available at Elsevier via https://doi.org/10.1016/j.compgeo.2017.02.020

Isogeometric Analysis of THM Coupled Processes in Ground Freezing

Yared W. Bekele[a,*], Hiroyuki Kyokawa[b], Arne M. Kvarving[c], Trond Kvamsdal[c,d], Steinar Nordal[a]

[a]*Department of Civil and Transport Engineering, NTNU, Trondheim, Norway*
[b]*Advanced Analysis Department, Civil Engineering Design Division, Kajima Corporation, Japan*
[c]*Department of Applied Mathematics, SINTEF ICT, Trondheim, Norway*
[d]*Department of Mathematical Sciences, NTNU, Trondheim, Norway*

Abstract

An isogeometric analysis (IGA) based numerical model is presented for simulation of thermo-hydro-mechanically (THM) coupled processes in ground freezing. The momentum, mass and energy conservation equations are derived based on porous media theory. The governing equations are supplemented by a saturation curve, a hydraulic conductivity model and constitutive equations. Variational and Galerkin formulation results in a highly nonlinear system of equations, which are solved using Newton-Raphson iteration. Numerical examples on isothermal consolidation in plane strain, one-dimensional freezing and heave due to a chilled pipeline are presented. Reasonably good agreements were observed between the IGA based heave simulations and experimental results.

Keywords: isogeometric analysis, THM coupling, porous media, ground freezing

1. Introduction

THM coupled numerical modeling is essential in several areas of geo/poromechanics to understand the multi-physical properties and responses of materials. The thermal, hydraulic and mechanical properties of such materials interact with each other resulting in a more complex overall behavior. A schematic representation of such interactions is shown in Figure 1. For instance hydraulic processes alter the thermal regime through convection, mechanical processes affect the hydraulic regime by changing the porosity and so on.

THM coupled numerical modeling has been widely applied in the geomechanics of the high temperature regime environment. Examples of such application areas include geothermal energy extraction, safety assessment of nuclear waste repositories, oil and gas reservoir engineering, underground energy storage and CO_2 sequestration; see for example Nowak *et al.* [24], Hudson *et al.* [7], Wang and Kolditz [37], Rutqvist *et al.* [27], Rutqvist *et al.* [28], Sanavia *et al.* [29], Wang *et al.* [38] and Tong *et al.* [35]. On the other hand, fully coupled THM modeling in frozen ground engineering is not as extensive. It is known that the freezing and thawing phenomena of ground can occur naturally, in cold regions, or artificially, as a construction technique in civil engineering. Some application areas in natural ground freezing and thawing include frost heave prediction, analysis and design of structures and foundations in cold regions and study of seasonal variation of temperature on the ground thermal properties. Artificial ground freezing on the other hand is a technology that has been successfully applied, over a long period of time, in the construction of structures on weak and/or unstable water-bearing grounds. Specific applications include the construction of tunnels of various purposes, the engineering of mines and pits, construction of underground storage facilities and the construction of foundations for industrial buildings on unstable ground. Artificial ground freezing is also used even in cold regions to control the seasonal thawing of frozen ground. The numerical proposed model in this paper will be applicable, within reason, to both natural and artificial ground freezing processes.

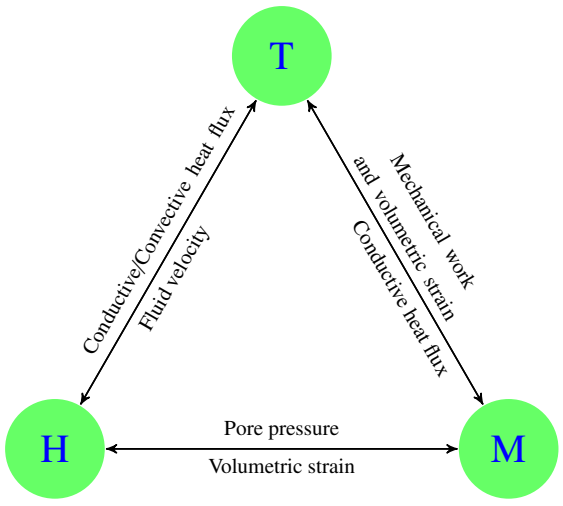

Figure 1: Schematic representation of Thermo-Hydro-Mechanical (THM) interactions, after [21].

*Corresponding author
Email addresses: yared.bekele@ntnu.no (Yared W. Bekele), kyokawa@kajima.com (Hiroyuki Kyokawa), arne.morten.kvarving@sintef.no (Arne M. Kvarving), trond.kvamsdal@math.ntnu.no (Trond Kvamsdal), steinar.nordal@ntnu.no (Steinar Nordal)

One of the earliest studies in the fully coupled THM modeling of frozen soils was presented by Mu and Ladanyi [19]. They made simplifying assumptions such as: the volume of soil particles remains constant in the freezing process, both unfrozen and frozen soil are isotropic, unfrozen soil is an elastic body with a constant Young's modulus where the Young's modulus and yield point are independent of the strain rate and confining pressure. The finite difference and finite element based simulation of unidirectional freezing was verified against experimental data. Selvadurai *et al.* [31] presented a computational model for frost heave with focus on soil-pipeline interaction and calibrated the proposed framework using one-dimensional frost heave tests. Another fully coupled THM model for frozen soil was proposed by Li *et al.* [13]. The effective stress equation for frozen soil was presented as a function of thermal stress, ice swelling and pore pressure. A simple thermo-elastic consolidation and numerical modeling of a pile foundation were studied by the proposed model. Nishimura *et al.* [23] presented the formulation and application of the THM coupled finite element analysis of frozen soil. The proposed fully coupled model was applied to the analysis of frost heave prediction and reasonably good agreements were obtained when compared with experimental data. Liu and Yu [14] proposed a fully coupled THM model under frost action where analogy of the soil water characteristic curve from unsaturated soils was applied to describe the freezing and drying processes. In the stress-strain field, the total strain was defined as the sum of elastic, thermal, phase change of water, change of matric potential and initial strains. Neaupane and Yamabe [20] also proposed a fully coupled THM model for a frozen medium and successfully applied it to simulate a freeze-thaw experiment. Dall'Amico *et al.* [5] proposed a robust and energy-conserving model for a freezing variably saturated soil. Based on the claim that the energy balance equation shows a strongly nonlinear behavior, they propose a globally-convergent Newton scheme where the energy equation is expressed based on internal energy. Wang *et al.* [39] discussed the numerical simulation of water-heat coupled movements in a seasonally frozen soil. Neaupane *et al.* [21] presented the simulation of a fully coupled THM system in freezing and thawing rock. Peng *et al.* [25] proposed a model for coupled heat, moisture and stress-field of saturated soil during freezing. Recent studies on the subject include consolidation of thawing permafrost by Qi *et al.* [26], a three-phase THM finite element model for freezing soils by Zhou and Meschke [40] and a fully coupled thermo-hydro-mechanical model for rock mass under freezing and thawing condition by Kang *et al.* [10]. Other related studies include those by Hansson *et al.* [6], Thomas *et al.* [34], Coussy [4], Newman and Wilson [22] and Micholawski and Zhu [16].

In this paper, a fully coupled thermo-hydro-mechanical (THM) finite element model for ground freezing and thawing is proposed. The governing equations of the THM model are derived based on porous media theory where the multiphase medium is approximated as a continuum. The governing equations of the model are supplemented by other state equations for temperature dependent variables such as degree of saturation and hydraulic conductivity. Isogeometric analysis using B-Splines is applied to solve the final system of equations numerically. The higher continuities of B-Splines result in a locally mass and energy conserving numerical implementation, unlike the standard finite element method. In addition, we are able to represent CAD (computer aided design) geometries in an "exact" manner by applying isogeometric analysis; geometries are only approximated through mesh generation when using the standard finite element method. This, for example, could be useful when simulating artificial ground freezing problems with circular pipe sections.

The paper is structured as follows. The modeling approach used for deriving the governing equations is briefly presented in Section 2. The derivation of the governing momentum, mass and energy balance equations for each phase and for the mixture is discussed in Section 3. The supplementary equations that complete the governing equations, such as the soil-water characteristic curve and the hydraulic conductivity model, are presented in Section 4. The fundamentals behind isogeometric analysis and its important features in our current context are discussed in Section 5.1. Variational formulation of the governing equations, spatial discretization using Galerkin's method and the numerical implementation are presented in Sections 5.2, 5.3 and 5.4, respectively. Numerical examples on isothermal consolidation, one-dimensional freezing and a frost heave problem are presented in Section 6 and the theoretical and numerical highlights of the proposed model are summarized in Section 7.

2. Modeling Approach

The three phase porous medium composed of solid grains, water and ice is approximated as a homogeneous continuum as shown in Figure 2.

According to porous media theory, the partial density of phase α is defined in terms of its volume fraction n_α and material density ρ^α as:

$$\rho^\alpha := n_\alpha \rho_\alpha \tag{1}$$

For a saturated frozen soil, the partial densities for the solid, water and ice phases are, according to equation (1), given by:

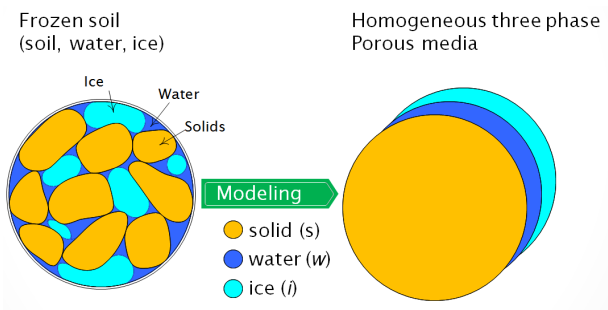

Figure 2: Multiphase porous medium modeled as a homogeneous continuum

$$\begin{aligned}\rho^{\mathrm{s}} &= n_{\mathrm{s}}\rho_{\mathrm{s}} = (1-n)\rho_{\mathrm{s}}\\ \rho^{\mathrm{w}} &= n_{\mathrm{w}}\rho_{\mathrm{w}} = nS_{\mathrm{w}}\rho_{\mathrm{w}} = n(1-S_{\mathrm{i}})\rho_{\mathrm{w}}\\ \rho^{\mathrm{i}} &= n_{\mathrm{i}}\rho_{\mathrm{i}} = nS_{\mathrm{i}}\rho_{\mathrm{i}}\end{aligned} \tag{2}$$

where n_{s}, n_{w} and n_{i} (with $n_{\mathrm{s}} + n_{\mathrm{w}} + n_{\mathrm{i}} = 1$) are the volume fractions of the solid, water and ice phases, respectively, n is the porosity, and S_{w} and S_{i} are the degrees of water and ice saturation respectively. For a fully saturated frozen soil, $S_{\mathrm{w}} + S_{\mathrm{i}} = 1$.

The total density of the porous medium is given as the sum of the partial densities of the component phases:

$$\rho = \rho^{\mathrm{s}} + \rho^{\mathrm{i}} + \rho^{\mathrm{w}} = (1-n)\rho_{\mathrm{s}} + nS_{\mathrm{i}}\rho_{\mathrm{i}} + nS_{\mathrm{w}}\rho_{\mathrm{w}} \tag{3}$$

The derivation of the governing equations is performed with respect to the solid phase and thus material time derivatives are extensively used in the derivations. The material time derivative of any differentiable function $f^{\alpha}(\boldsymbol{x}, t)$, varying in space $\boldsymbol{x}$ and in time t, referring to a moving particle of the α phase is given by:

$$\frac{\mathrm{D}_{\alpha} f^{\alpha}}{\mathrm{D}t} := \frac{\partial f^{\alpha}}{\partial t} + \nabla f^{\alpha} \cdot \boldsymbol{v}^{\alpha}. \tag{4}$$

In this case, material time derivatives of properties $f^{\alpha}(\boldsymbol{x}, t)$ relating to the water and ice phases are performed with respect to the solid phase. It can be shown that the material time derivative of $f^{\alpha}(\boldsymbol{x}, t)$ of phase $\alpha \in (\mathrm{w}, \mathrm{i})$ with respect to the solid phase is given by:

$$\frac{\mathrm{D}_{\mathrm{s}} f^{\alpha}}{\mathrm{D}t} = \frac{\mathrm{D}_{\alpha} f^{\alpha}}{\mathrm{D}t} + \nabla f^{\alpha} \cdot (\boldsymbol{v}^{\mathrm{s}} - \boldsymbol{v}^{\alpha}) \tag{5}$$

where $\boldsymbol{v}^{\mathrm{s}} - \boldsymbol{v}^{\alpha}$ is the relative velocity of phase α with respect to the solid phase.

3. Governing Equations

In this section, the governing partial differential equations of the proposed THM coupled model are presented. The three main governing equations for the saturated frozen soil are the linear momentum balance equation, the mass balance equation and the energy balance equation. These governing equations are supplemented by the modified Clausius-Clapeyron equation for thermodynamic equilibrium, the soil-water characteristic curve for the degree of water saturation as a function of pressure and temperature and a constitutive law for the stress-strain behavior of the solid skeleton.

3.1. Linear Momentum Balance Equation

The linear momentum balance equation is the equation of motion or equilibrium equation for the mixture. For a phase α of the mixture, it is given by:

$$\nabla \cdot \boldsymbol{\sigma}^{\alpha} + \rho^{\alpha}\boldsymbol{b}^{\alpha} + \sum_{\beta} \boldsymbol{P}^{\beta\alpha} = \rho_{\alpha} \frac{\mathrm{D}_{\alpha}\boldsymbol{v}^{\alpha}}{\mathrm{D}t} \tag{6}$$

where $\boldsymbol{\sigma}^{\alpha}$ is the partial stress of phase α, $\boldsymbol{P}^{\beta\alpha}$ are the interphase interactive forces between phase α and phase β and $\boldsymbol{b}^{\alpha}$ are the body forces for phase α. The equilibrium equation for the whole mixture is obtained as a summation of the individual equilibrium equation of each phase. Assuming a static problem, this results in:

$$\nabla \cdot \boldsymbol{\sigma} + \rho\boldsymbol{b} = \boldsymbol{0} \tag{7}$$

where $\boldsymbol{\sigma}$ are the total stresses and $\boldsymbol{b}$ are the body forces. The Bishop type effective stress in terms of the pore water and ice pressures p^{w} and p^{i} is given by:

$$\boldsymbol{\sigma'} = \boldsymbol{\sigma} + p^{\mathrm{w}}\boldsymbol{I} + S_{\mathrm{i}}(p^{\mathrm{i}} - p^{\mathrm{w}})\boldsymbol{I} \tag{8}$$

where $\boldsymbol{I}$ is an identity matrix. The mechanical equilibrium equation in terms of the effective stresses can thus be written as:

$$\nabla \cdot \boldsymbol{\sigma'} - \nabla p^{\mathrm{w}} - \nabla(S_{\mathrm{i}}(p^{\mathrm{i}} - p^{\mathrm{w}})) + \rho\boldsymbol{b} = \boldsymbol{0}. \tag{9}$$

The effective stress is further linked to strain via a constitutive model. A simple constitutive model is presented in Section 4.4.

3.2. Mass Balance Equation

The general form of the mass balance equation for a phase α, considering phase change from phases β to phase α (with a mass exchange per unit volume of $M^{\beta\alpha}$), is given by:

$$\frac{\mathrm{D}_{\alpha}\rho^{\alpha}}{\mathrm{D}t} + \rho^{\alpha}\nabla \cdot \boldsymbol{v}^{\alpha} + \sum_{\beta} M^{\beta\alpha} = 0. \tag{10}$$

The mass balance equation for each phase is then derived and the equations for water and ice are derived with respect to the solid phase. The mass balance equation for the solid phase with the assumption of incompressible solid grains gives the time change of porosity as a function of solid displacement as:

$$\frac{\mathrm{D}_{\mathrm{s}}\rho^{\mathrm{s}}}{\mathrm{D}t} = 0 \Rightarrow \frac{\mathrm{D}_{\mathrm{s}} n}{\mathrm{D}t} = (1-n)\nabla \cdot \boldsymbol{v}^{\mathrm{s}}. \tag{11}$$

Summation of the individual mass balance equations for water and ice, together with the use of equation (11), gives the mass balance equation for the pores as:

$$(\rho_{\mathrm{w}}S_{\mathrm{w}} + \rho_{\mathrm{i}}S_{\mathrm{i}})\nabla \cdot \boldsymbol{v}^{\mathrm{s}} + n(\rho_{\mathrm{w}} - \rho_{\mathrm{i}})\frac{\mathrm{D}_{\mathrm{s}}S_{\mathrm{w}}}{\mathrm{D}t} + \rho_{\mathrm{w}}\nabla \cdot \boldsymbol{w} + \rho_{\mathrm{i}}\nabla \cdot \boldsymbol{w'} = 0 \tag{12}$$

where we have used the fact that the mass exchanges between water and ice cancel each other out i.e. $\Delta M_{iw} + \Delta M_{wi} = 0$. We have assumed herein that all phases are incompressible (no volume change under isotropic compression) and that the spatial variation of density (density gradient) is negligible for all phases. In Eq. (12), $\boldsymbol{w}$ and $\boldsymbol{w'}$ represent the water and ice fluxes relative to the solid phase. The water flux, for flow driven by pressure gradient and gravity, can be expressed using Darcy's law as:

$$\boldsymbol{w} = -\frac{1}{\gamma^{\mathrm{w}}}\boldsymbol{k}\left(\nabla p^{\mathrm{w}} - \rho_{\mathrm{w}}\boldsymbol{b}\right) \tag{13}$$

where $\boldsymbol{k}$ is the hydraulic conductivity matrix, which is a function of both pressure and temperature, and γ^{w} is the unit weight

of water. A relative hydraulic conductivity model is required to control the evolution of $\boldsymbol{k}$ and this is presented in Section 4.3.

The ice flux relative to the solid phase is usually neglected but a relationship between $\boldsymbol{w}'$ and $\boldsymbol{w}$ can be derived such that:

$$\boldsymbol{w}' = \frac{S_\mathrm{i}}{S_\mathrm{w}}\boldsymbol{w} = \theta\boldsymbol{w}. \tag{14}$$

The above equation implies that some water flux is used for phase change between water and ice according to the current degree of ice saturation.

3.3. Energy Balance Equation

The general energy balance equation for a phase α, considering energy change due to phase change from phase β to phase α, is given by:

$$\rho^\alpha \frac{\mathrm{D}_\alpha e^\alpha}{\mathrm{D}t} + e^\alpha \left(- \sum_\beta M^{\beta\alpha} \right) + \Delta Q_\alpha^\mathrm{ph} = -\nabla \cdot \boldsymbol{q}^\alpha + Q^\alpha \tag{15}$$

where e^α is the specific internal energy of phase α, Q_α^ph is the additional energy causing phase change, $\boldsymbol{q}^\alpha$ is the conductive heat flux for phase α and Q_α is the sink or source term of energy for the same phase, which can be assumed to be equal to zero for a closed system. The internal energy of phase α, in terms of its heat capacity c_α and the temperature T is defined as:

$$e^\alpha := c_\alpha T. \tag{16}$$

Accordingly, the specific internal energies for the solid, water and ice phases can thus be expressed as:

$$e^\mathrm{s} = c_\mathrm{s} T, \qquad e^\mathrm{w} = c_\mathrm{w} T, \qquad e^\mathrm{i} = c_\mathrm{i} T \tag{17}$$

where c_s, c_w and c_i are the respective specific heat capacities for each phase. After formulating the specific energy balance equations for the solid, water and ice phases and making the same assumptions as in the mass balance equation, summation of the individual equations gives the energy balance equation for the three-phase medium as:

$$(\rho c)_\mathrm{eff} \frac{\mathrm{D}_\mathrm{s} T}{\mathrm{D}t} + \boldsymbol{a} \cdot \nabla T + L_\mathrm{f} \xi \frac{\mathrm{D}_\mathrm{s} S_\mathrm{w}}{\mathrm{D}t} = -\nabla \cdot \boldsymbol{q} + Q \tag{18}$$

where $\boldsymbol{a} = (\rho c)_\mathrm{adv} \boldsymbol{w}$ is an advective heat transfer vector, L_f is the latent heat of fusion and we have the volumetric parameter ξ as:

$$\xi = \frac{n\rho_\mathrm{i}}{S_\mathrm{w} + \frac{\rho_\mathrm{i}}{\rho_\mathrm{w}} S_\mathrm{i}}. \tag{19}$$

The effective heat capacity for the mixture and the advective heat transfer coefficient are given by:

$$\begin{aligned} (\rho c)_\mathrm{eff} &= \rho^\mathrm{s} c_\mathrm{s} + \rho^\mathrm{w} c_\mathrm{w} + \rho^\mathrm{i} c_\mathrm{i} \\ &= (1-n)\rho_\mathrm{s} c_\mathrm{s} + n S_\mathrm{w} \rho_\mathrm{w} c_\mathrm{w} + n S_\mathrm{i} \rho_\mathrm{i} c_\mathrm{i} \\ (\rho c)_\mathrm{adv} &= \rho_\mathrm{w} c_\mathrm{w} + \theta \rho_\mathrm{i} c_\mathrm{i} \end{aligned} \tag{20}$$

The total conductive heat flux, assuming isotropic thermal conductivity, can be expressed using Fourier's law as:

$$\boldsymbol{q} = -\lambda \nabla T. \tag{21}$$

The overall thermal conductivity λ for the multiphase porous medium can be obtained as the geometric mean of the individual thermal conductivities using, [2]:

$$\lambda = \lambda_\mathrm{s}^{1-n} \cdot \lambda_\mathrm{w}^{nS_\mathrm{w}} \cdot \lambda_\mathrm{i}^{n(1-S_\mathrm{w})} \tag{22}$$

where λ_s, λ_w and λ_i are the thermal conductivities of solid, water and ice respectively.

The current paper focuses on a saturated frozen soil (solid, water and ice phases) and the governing equations are derived accordingly. Unsaturated soils under freezing and thawing conditions involve solid, water, air and ice phases. Numerical modeling of problems involving unsaturated soils requires modification of the governing equations considering all the phases involved. For instance, the presence of an air phase requires modification of the mass balance equation for the pores by considering the individual mass balance equation for the air phase. The introduction of air pressure due to the air phase also necessitates modification of the effective stress formulation which is used in the linear momentum balance equation. The energy balance equation also requires modification to consider the effects of the air phase on the heat capacity and heat transfer phenomena in the soil.

4. Supplementary Equations

4.1. Modified Clausius-Clapeyron Equation

The thermodynamic equilibrium between ice and soil in a freezing soil is described by the modified Clausius-Clapeyron equation, see [15]. The ice and water pressures in this equation are related by:

$$p^\mathrm{i} = \frac{\rho_\mathrm{i}}{\rho_\mathrm{w}} p^\mathrm{w} - \rho_\mathrm{i} L_\mathrm{f} \ln\left(\frac{T}{T_0}\right) \tag{23}$$

where T_o=273.15 K is the reference temperature and the relation is derived considering atmospheric pressure conditions. The equation is valid for practical temperature and pressure ranges of interest, [18].

4.2. Soil-Water Characteristic Curve

The other most important relation required to supplement the governing equations is the degree of water saturation as a function of pressure and temperature, i.e. $S_\mathrm{w} = f(p^\mathrm{w}, T)$, also known as the soil-water characteristic curve in unsaturated soil mechanics terminology. Based on van Genuchten's [36] model for unsaturated soils, and as modified in Nishimura *et al.* [23] and Zhou and Meschke [40], the soil-water characteristic curve for freezing and thawing porous media may be written as:

$$S_\mathrm{w} = 1 - S_\mathrm{i}^{max} \left[1 - \left\{ 1 + \left(\alpha (p^\mathrm{i} - p^\mathrm{w}) \right)^\beta \right\}^{-\gamma} \right] \tag{24}$$

where S_i^{max} is the maximum degree of ice saturation for numerical reasons and α, β and γ are model parameters. Using the Clausius-Clapeyron equation, Eq. (23), which expresses p^i in terms of p^w, into Eq. (24) results in:

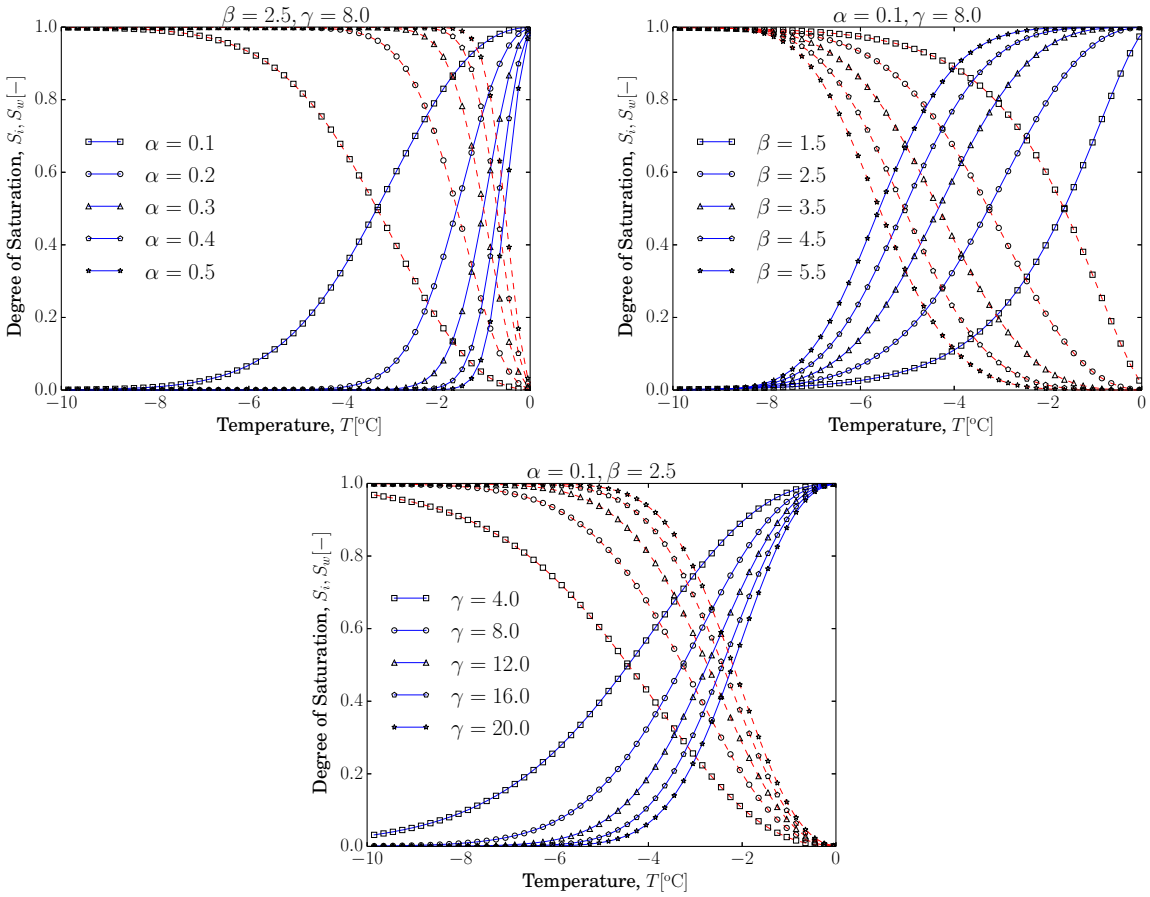

Figure 3: Effects of the saturation model parameters α, β and γ: Degree of water and ice saturation versus temperature for different combinations of the model parameters. The solid lines represent S_w and the dashed lines are for S_i. The parameter α has a unit of MPa^{-1} while β and γ are dimensionless.

$$S_w = 1 - S_i^{max}\left[1 - \left\{1 + \left[\alpha\left((\frac{\rho_i}{\rho_w} - 1)p^w - \rho_i L_f \ln(\frac{T}{T_o})\right)\right]^{\beta}\right\}^{-\gamma}\right]. \tag{25}$$

The rate of change of S_w can thus be expressed as:

$$\frac{\partial S_w}{\partial t} = \frac{\partial S_w}{\partial p^w}\frac{\partial p^w}{\partial t} + \frac{\partial S_w}{\partial T}\frac{\partial T}{\partial t} = S_p\frac{\partial p^w}{\partial t} + S_T\frac{\partial T}{\partial t} \tag{26}$$

where S_p and S_T may, respectively, be referred to as isothermal and non-isothermal water capacities.

The model parameters α, β and γ can be selected for a given material based on experimental data. The effects of these model parameters on the degree of saturation are illustrated in the plots in Figure 3 as a function of temperature. A fixed value is used for the pore water pressure p^w and it can be shown that the effect of p^w on the degree of water saturation S_w is very limited compared to temperature. The variations in the saturation plots for different saturation model parameters indicate the possibility of representing the behaviour of various types of soils, fine-grained or coarse-grained, during freezing and thawing. Different soil types may become ice-rich or ice-poor during freezing. For instance for $\beta = 2.5$ and $\gamma = 8.0$, the saturation curve with $\alpha = 0.1$ MPa^{-1} represents a soil that freezes slowly whereas the one with $\alpha = 0.5$ MPa^{-1} represents a soil that freezes quickly.

4.3. Hydraulic Conductivity Model

The hydraulic conductivity of the porous medium changes continuously during the freezing/thawing process depending on the degree of water saturation i.e. as a function of temperature. To calculate the hydraulic conductivity at a given temperature, a relative hydraulic conductivity parameter is introduced into Darcy's law, [23]. The modified Darcy's law and the corresponding relative hydraulic conductivity parameter are given by:

$$\begin{aligned} \boldsymbol{w} &= -\frac{k_r}{\gamma^w}\boldsymbol{k}\left(\nabla p^w - \rho_w \boldsymbol{b}\right) \\ k_r &= \sqrt{S_w}\left[1 - \left(1 - S_w^{1/m}\right)^m\right]^2 \end{aligned} \tag{27}$$

where m is a model parameter. The variation of k_r with degree of water saturation for selected values of m is plotted and shown in Figure 4. The model parameter may be selected for a given soil base on experimental data of hydraulic conductivity. For

example, the curve for $m = 0.5$ may represent an ice-rich soil whereas the one for $m = 2.5$ fits better for an ice-poor soil.

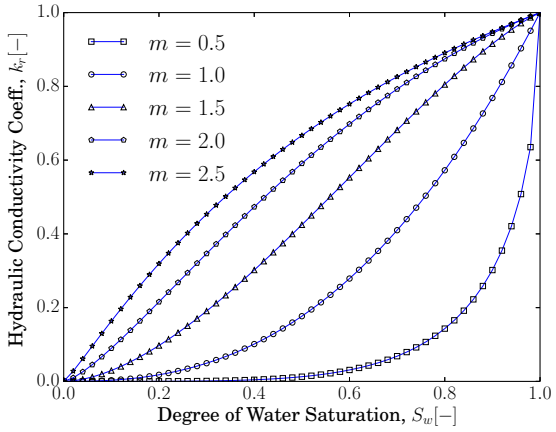

Figure 4: Relative hydraulic conductivity versus degree of water saturation.

4.4. Constitutive Equations

The general stress-strain relation in incremental form can be written as:

$$\mathrm{d}\boldsymbol{\sigma'} = \boldsymbol{D}(\mathrm{d}\boldsymbol{\varepsilon} - \mathrm{d}\boldsymbol{\varepsilon}^{\mathrm{ph}} - \mathrm{d}\boldsymbol{\varepsilon}^{\mathrm{T}}) \tag{28}$$

where $d\boldsymbol{\sigma'}$ is the effective stress increment, $\boldsymbol{D}$ is the constitutive tangent stiffness tensor, $\mathrm{d}\boldsymbol{\varepsilon}$ is the total strain increment, $\mathrm{d}\boldsymbol{\varepsilon}^{\mathrm{ph}}$ is the strain increment due to phase change and $\mathrm{d}\boldsymbol{\varepsilon}^{\mathrm{T}}$ is the thermal strain increment. The thermal strain is usually very small when compared to the strain due to phase change and may be neglected.

The constitutive equation proposed for the soil skeleton here is a simple nonlinear elastic relation with temperature dependent parameters. The tangent stiffness for linear elasticity (for stresses and strains in Voigt notation) is given by

$$\boldsymbol{D} = \frac{E}{(1+\nu)(1-2\nu)} \begin{bmatrix} \boldsymbol{D}_{11} & \boldsymbol{0} \\ \boldsymbol{0} & \boldsymbol{D}_{22} \end{bmatrix} \tag{29}$$

where

$$\begin{aligned} \boldsymbol{D}_{11} &= (1-2\nu)\boldsymbol{I} + \nu\boldsymbol{I}, \\ \boldsymbol{D}_{22} &= \frac{1-2\nu}{2}\boldsymbol{I}, \end{aligned} \tag{30}$$

where E is the Young's modulus, ν is the Poisson's ratio and $\boldsymbol{I}$ is a matrix of ones. These strength parameters are temperature dependent and simple nonlinear relations are derived as a function of degree of saturation, which is a function of temperature according to the soil-water characteristic curve. The Young's modulus E of the porous medium at a given temperature may be expressed as:

$$E = \left(\frac{E_{\mathrm{i}}}{E_{\mathrm{s}}}\right)^{S_{\mathrm{i}}^{\eta}} E_{\mathrm{s}} \tag{31}$$

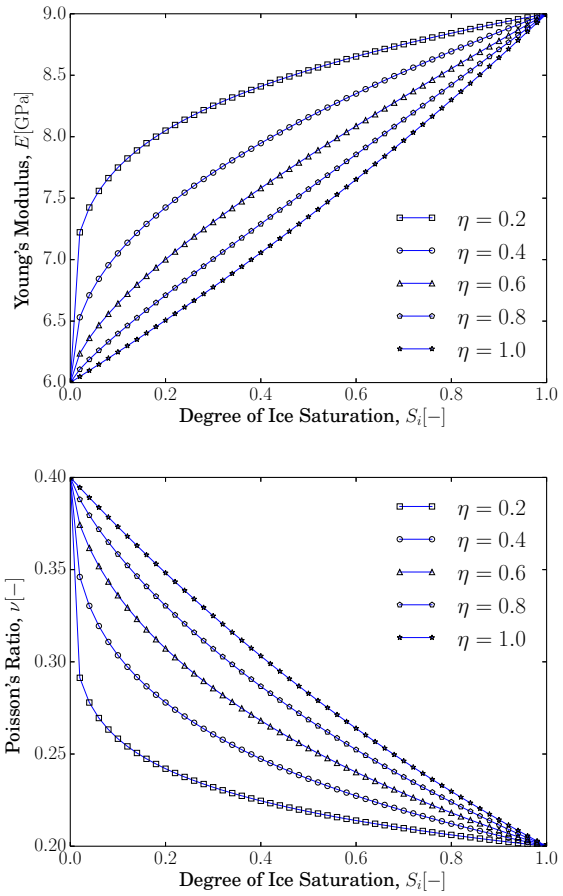

Figure 5: Strength parameters E and ν as a function of degree of ice saturation.

where E_{i} and E_{s} are the Young's moduli of ice and solid skeleton respectively, S_{i} is the degree of ice saturation and η is a model parameter. A similar expression for the Poisson's ratio ν of the porous medium as a function of the Poisson's ratios of ice, ν_{i}, and solid skeleton, ν_{s}, is given by:

$$\nu = \left(\frac{\nu_{\mathrm{i}}}{\nu_{\mathrm{s}}}\right)^{S_{\mathrm{i}}^{\eta}} \nu_{\mathrm{s}}. \tag{32}$$

The strength parameter η may be chosen for a given material based on experimental data. If we assume for example that $E_{\mathrm{s}} = 6$ GPa, $E_{\mathrm{i}} = 9$ GPa, $\nu_{\mathrm{s}} = 0.4$ and $\nu_{\mathrm{i}} = 0.2$, the overall Young's modulus E and Poisson's ratio ν may be plotted as a function of degree of ice saturation for different values of η, as shown in Figure 5. Depending on the initial porosity of the soil and its freezing characteristics, the strength of the soil after freezing is initiated may increase at a different rate. As an example, the curve for a strength model parameter $\eta = 0.2$ shows a faster increase in strength when freezing is initiated than the one for $\eta = 1.0$.

The thermal strain increment as a function of the thermal expansion coefficient of the solid skeleton and temperature increment is given by:

$$\mathrm{d}\boldsymbol{\varepsilon}^T = \frac{\alpha_\mathrm{s}}{3}\mathrm{d}T\boldsymbol{I}. \tag{33}$$

The volume expansion of the soil due to phase change is accounted for by the strain due to phase change, $\boldsymbol{\varepsilon}^{\mathrm{ph}}$, and is a function of the porosity and the degree of ice saturation. An expression for $\boldsymbol{\varepsilon}_{\mathrm{ph}}$ can be derived by formulating the volumetric strains $\varepsilon_\mathrm{v}^{\mathrm{ph}}$ as a function of n and S_i. Assuming isotropic expansion, the rate of volumetric expansion may be derived from the mass balance of ice and water during phase change, i.e. $\frac{\partial}{\partial t}\{(\rho_\mathrm{w}V_\mathrm{w}) + (\rho_\mathrm{i}V_\mathrm{i})\} = 0$, to give:

$$\dot{\varepsilon}_\mathrm{v}^{\mathrm{ph}} = \frac{n(\rho_\mathrm{w} - \rho_\mathrm{i})}{\rho_\mathrm{w}S_\mathrm{w} + \rho_\mathrm{i}S_\mathrm{i}}\frac{\mathrm{D}_\mathrm{s}S_\mathrm{i}}{\mathrm{D}t}. \tag{34}$$

The incremental strain due to phase change may then be written as:

$$d\boldsymbol{\varepsilon}^{\mathrm{ph}} = \frac{1}{3}\left(\frac{\partial\varepsilon_\mathrm{v}^{\mathrm{ph}}}{\partial S_\mathrm{i}}dS_\mathrm{i}\right)\boldsymbol{I}. \tag{35}$$

5. Isogeometric Analysis

5.1. Introduction

Since its first introduction by Hughes *et al*. [9], isogeometric analysis (IGA) has been successfully applied to several areas of engineering mechanics problems. The fundamental aim for the introduction of IGA was the idea of bridging the gap between finite element analysis (FEA) and computer-aided design (CAD). The main concept behind the method is the application of the same basis functions used in CAD for performing finite element analysis. In the process of its application to various engineering problems, IGA has shown advantages over the conventional finite element method, for instance the ease of performing finite element analysis using higher order polynomials.

We briefly present the fundamentals behind B-Splines and NURBS in the next section and highlight the features of IGA that are important in our context.

5.1.1. Fundamentals on B-Splines and NURBS

We start the discussion on B-Splines and NURBS by first defining a *knot vector*. A knot vector in one dimension is a non-decreasing set of coordinates in the parameter space, written $\Xi = \{\xi_1, \xi_2, ..., \xi_{n+p+1}\}$, where $\xi_i \in \mathbb{R}$ is the i^{th} knot, i is the knot index, $i = 1, 2, ..., n + p + 1$, p is the polynomial order, and n is the number of basis functions. Knot vectors may be uniform or non-uniform depending on whether the knots are equally spaced in the parameter space or not.

A univariate B-Spline curve is parametrized by a linear combination of n B-Spline basis functions, $\{N_{i,p}\}_{i=1}^{n}$. The B-Spline basis functions are recursively defined starting with piecewise constants ($p = 0$):

$$N_{i,0}(\xi) = \begin{cases} 1 & \text{if } \xi_i \le \xi < \xi_{i+1} \\ 0 & \text{otherwise.} \end{cases} \tag{36}$$

For higher-order polynomial degrees ($p \ge 1$), the basis functions are defined by the Cox-de Boor recursion formula:

$$N_{i,p}(\xi) = \frac{\xi - \xi_i}{\xi_{i+p} - \xi_i}N_{i,p-1}(\xi) + \frac{\xi_{i+p+1} - \xi}{\xi_{i+p+1} - \xi_{i+1}}N_{i+1,p-1}(\xi). \tag{37}$$

B-Spline geometries, curves, surfaces and solids, are constructed from a linear combination of B-Spline basis functions. Given n basis functions $N_{i,p}$ and corresponding control points $\boldsymbol{P}_i \in \mathbb{R}^d, i = 1, 2, ..., n$, a piecewise polynomial B-Spline curve is given by:

$$\boldsymbol{C}(\xi) = \sum_{i=1}^{n} N_{i,p}(\xi)\boldsymbol{P}_i. \tag{38}$$

Similarly, for a given control net $\boldsymbol{P}_{i,j}, i = 1, 2, ..., n, j = 1, 2, ..., m$, polynomial orders p and q, and knot vectors $\Xi = \{\xi_1, \xi_2, ..., \xi_{n+p+1}\}$, and $\mathcal{H} = \{\eta_1, \eta_2, ..., \eta_{m+q+1}\}$, a tensor product B-Spline surface is defined by:

$$\boldsymbol{S}(\xi, \eta) = \sum_{i=1}^{n}\sum_{j=1}^{m} N_{i,p}(\xi)M_{j,q}(\eta)\boldsymbol{P}_{i,j}. \tag{39}$$

B-Spline solids are defined in a similar way as B-Spline surfaces from tensor products over a control lattice.

NURBS are built from B-Splines to represent a wide array of objects that cannot be exactly represented by polynomials. A NURBS entity in $\mathbb{R}^d$ is obtained by the projective transformation of a B-Spline entity in $\mathbb{R}^{d+1}$. The control points for the NURBS geometry are found by performing exactly the same projective transformation to the control points of the B-Spline geometry.

A detailed treatment of B-Splines and NURBS can be referred from Cottrell *et al.* [3].

5.1.2. Important Features in Current Context

IGA has a number of advantages over FEA such as the ability to represent exact CAD geometries of structures or domains during analysis, non-negative basis functions and isoparametric mapping at patch level. In the context of the current work, we focus on the features of IGA that are especially important. These features are the improved continuity of filed variables because of the smoothness of the basis functions and the ability to perform simulations with high continuity and high regularity meshes. Next, we will look into these features closely.

Continuity: One of the most distinctive and powerful features of IGA is that the basis functions will be C^{p-m} continuous across knot spans (analogous to elements in FEA), where p is the polynomial degree and m is the multiplicity of the knot. This means that the continuity across knot spans can be controlled by the proper choice of p and m. The continuity can be decreased by repeating a knot - important to model non-smooth geometry features or to facilitate the application of boundary conditions. For instance, quadratic ($p = 2$) splines are C^1 continuous over non-repeated knots while quadratic Lagrange finite element bases are only C^0 continuous. If we consider the quartic ($p = 4$) basis functions constructed from the open, non-uniform knot vector

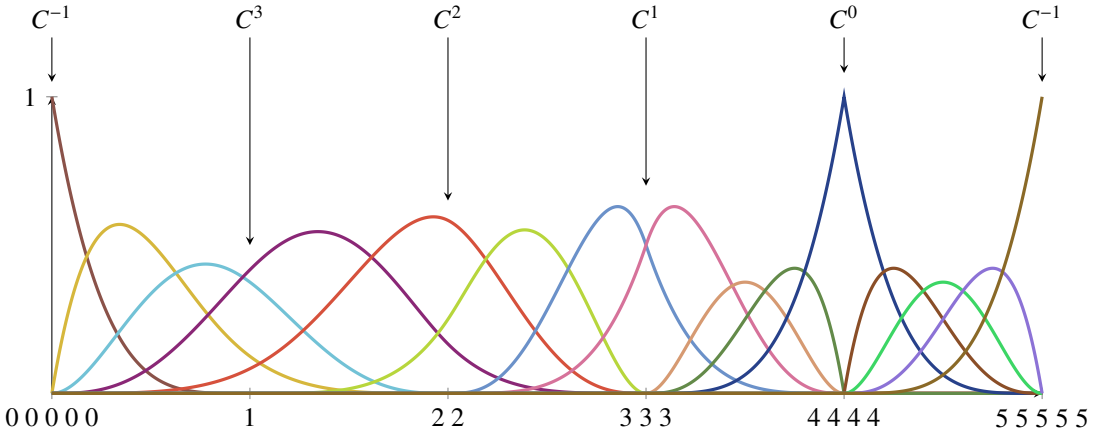

Figure 6: Different continuities across knot spans, after [3].

$\Xi = \{0,0,0,0,0,1,2,2,3,3,3,4,4,4,4,5,5,5,5,5\}$, we get different continuities across knot spans as shown in Figure 6.

k-refinement: IGA and FEA both allow *h*- and *p*-refinements i.e. increasing the number of knot spans by knot insertion (increasing the number of elements in FEA) and raising the polynomial order. The non-commutativity of knot insertion and polynomial order elevation results in a type of refinement that is unique to IGA, called *k*-refinement. This is achieved by performing polynomial order elevation followed by knot insertion. This results in a high continuity mesh with the least number of degrees of freedom i.e. high regularity.

5.1.3. Mixed isogeometric formulation

A mixed formulation is constructed by first defining the knot vectors and basis functions defining the geometry of the domain. The polynomial order defining the geometry is used as the polynomial degree for one of the field variables and is raised by the desired degree for the other field variable. In our context, the polynomial orders for the pressure and temperature, p_p and p_T, are defined by the geometry construction and the polynomial order for the displacement, p_u, is raised by one. All polynomial orders can then be raised to the desired degree starting from the initial definition. For example, a simple two-dimensional geometry defined by the knot vectors $\Xi = \{0,0,1,1\}$ and $\mathcal{H} = \{0,0,1,1\}$ implies $p_\mathrm{p} = p_\mathrm{T} = 1$ and $p_\mathrm{u} = 2$ with 4 and 9 control points, respectively. The number of control points, location of degrees of freedom in IGA, on a B-Spline surface for different polynomial degrees is shown in Figure 7.

5.2. Variational Formulation

We first define the initial and boundary conditions before presenting the variational formulation of the governing equations. The initial conditions for the displacement, pore water pressure and temperature at time $t = 0$ are:

$$\boldsymbol{u} = \boldsymbol{u}_\mathrm{o} \qquad p^\mathrm{w} = p^\mathrm{w}_\mathrm{o} \qquad T = T_\mathrm{o} \qquad \text{in } \Omega \text{ and on } \Gamma \tag{40}$$

where Ω and Γ are the domain and its boundary, respectively. The boundary conditions could be of Dirichlet type on Γ_D or Neumann type (fluxes and tractions) on Γ_N, where $\Gamma_D \cup \Gamma_N = \Gamma$. The Dirichlet boundary conditions may be defined as:

$$\begin{cases} \boldsymbol{u} = \overline{\boldsymbol{u}} & \text{on } \Gamma^\mathrm{u}_D \\ p^\mathrm{w} = \overline{p}^\mathrm{w} & \text{on } \Gamma^\mathrm{p}_D \\ T = \overline{T} & \text{on } \Gamma^\mathrm{T}_D. \end{cases} \tag{41}$$

The Neumann boundary conditions are defined as:

$$\begin{cases} \boldsymbol{\sigma} \cdot \boldsymbol{n} = \overline{\boldsymbol{t}} & \text{on } \Gamma^\mathrm{u}_N \\ \boldsymbol{w} \cdot \boldsymbol{n} = \overline{q}^\mathrm{w} & \text{on } \Gamma^\mathrm{p}_N \\ \boldsymbol{q} \cdot \boldsymbol{n} = \overline{q}^\mathrm{T} + \lambda_\mathrm{e}(T - T_\mathrm{e}) & \text{on } \Gamma^\mathrm{T}_N \end{cases} \tag{42}$$

where $\overline{\boldsymbol{t}}$ is the traction boundary condition and $\boldsymbol{n}$ is the outward unit normal vector to the boundary. The water and heat fluxes at the boundary are represented by $\overline{q}^\mathrm{w}$ and $\overline{q}^\mathrm{T}$, respectively. The thermal conductivity and temperature of the surrounding environment are denoted by λ_e and T_e, respectively.

We can now derive the weak formulations of the three main governing balance equations, Eq. (7), (12) and (18). Multiplying the rate form of the linear momentum balance equation by arbitrary velocities $\delta\boldsymbol{v}$, integrating over the domain Ω and applying the divergence theorem gives the weak form as:

$$\int_\Omega \dot{\boldsymbol{\sigma}} \cdot \nabla \cdot \delta\boldsymbol{v} \mathrm{d}\Omega = \int_{\Gamma^\mathrm{u}_N} \dot{\overline{\boldsymbol{t}}} \delta\boldsymbol{v} \mathrm{d}\Gamma \tag{43}$$

where $\overline{\boldsymbol{t}}$ is the Neumann traction on the boundary Γ^u_N, $\dot{\boldsymbol{\sigma}} = \frac{\partial \boldsymbol{\sigma}}{\partial t}$ and $\dot{\overline{\boldsymbol{t}}} = \frac{\partial \overline{\boldsymbol{t}}}{\partial t}$. The rate of change of the total stress is derived from the effective stress relationship. Using the constitutive relation given in Eq. (28) into the effective stress formulation in Eq. (8), a generic form of the rate of change of total stress can be derived as:

$$\dot{\boldsymbol{\sigma}} = \boldsymbol{D}\dot{\boldsymbol{\varepsilon}} + \left(\frac{\partial \boldsymbol{\sigma}}{\partial p^\mathrm{w}} - \boldsymbol{D}\frac{\partial \boldsymbol{\varepsilon}^\mathrm{ph}}{\partial p^\mathrm{w}}\right)\frac{\partial p^\mathrm{w}}{\partial t} + \left(\frac{\partial \boldsymbol{\sigma}}{\partial T} - \boldsymbol{D}\frac{\partial \boldsymbol{\varepsilon}^\mathrm{ph}}{\partial T}\right)\frac{\partial T}{\partial t} \tag{44}$$

wherein we have neglected thermal and other strains. The weak form of the equilibrium equation can now be written as:

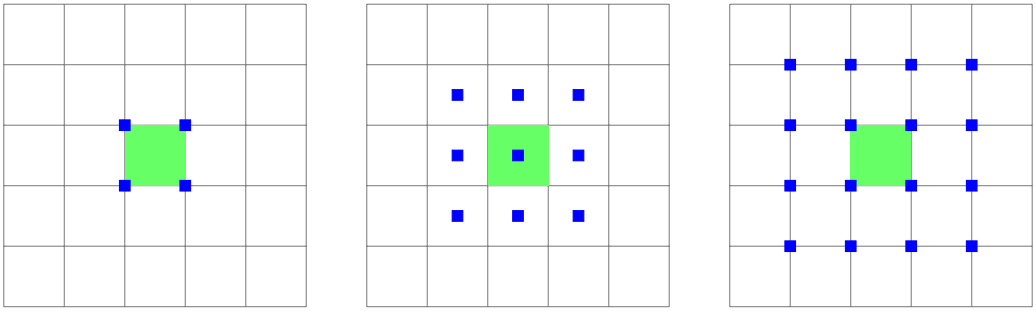

Figure 7: Number of control points for a given element on a simple B-Spline surface with different polynomial degrees. The element is highlighted and the blue squares represent control points.

$$\int_\Omega \left[\boldsymbol{D}\dot{\boldsymbol{\varepsilon}} + \left(\frac{\partial \boldsymbol{\sigma}}{\partial p^{\mathrm{w}}} - \boldsymbol{D}\frac{\partial \boldsymbol{\varepsilon}^{\mathrm{ph}}}{\partial p^{\mathrm{w}}} \right) \frac{\partial p^{\mathrm{w}}}{\partial t} + \left(\frac{\partial \boldsymbol{\sigma}}{\partial T} - \boldsymbol{D}\frac{\partial \boldsymbol{\varepsilon}^{\mathrm{ph}}}{\partial T} \right) \frac{\partial T}{\partial t} \right] \nabla \cdot \delta \boldsymbol{v} \mathrm{d}\Omega = \int_{\Gamma_N^{\mathrm{u}}} \dot{\bar{\boldsymbol{t}}} \delta \boldsymbol{v} \mathrm{d}\Gamma. \quad (45)$$

The weak form of the mass balance equation is derived by multiplying Eq. (12) by an arbitrary pressure δp and integrating over the domain Ω to give:

$$\int_\Omega \left[(\rho_{\mathrm{w}} S_{\mathrm{w}} + \rho_{\mathrm{i}} S_{\mathrm{i}}) \nabla \cdot \boldsymbol{v}^{\mathrm{s}} + n(\rho_{\mathrm{w}} - \rho_{\mathrm{i}}) \frac{\mathrm{D}_{\mathrm{s}} S_{\mathrm{w}}}{\mathrm{D}t} + (\rho_{\mathrm{w}} + \theta \rho_{\mathrm{i}}) \nabla \cdot \boldsymbol{w} \right] \delta p \mathrm{d}\Omega = 0. \quad (46)$$

Applying the divergence theorem, using Eq. (26) and rearranging gives the weak form of the mass balance equation as:

$$\begin{aligned} &\int_\Omega \frac{\rho_{\mathrm{w}} S_{\mathrm{w}} + \rho_{\mathrm{i}} S_{\mathrm{i}}}{\rho_{\mathrm{w}} + \theta \rho_{\mathrm{i}}} \nabla \cdot \boldsymbol{v}^{\mathrm{s}} \delta p \mathrm{d}\Omega + \int_\Omega \frac{n(\rho_{\mathrm{w}} - \rho_{\mathrm{i}})}{\rho_{\mathrm{w}} + \theta \rho_{\mathrm{i}}} S_{\mathrm{p}} \frac{\partial p^{\mathrm{w}}}{\partial t} \delta p \mathrm{d}\Omega \\ &+ \int_\Omega \frac{n(\rho_{\mathrm{w}} - \rho_{\mathrm{i}})}{\rho_{\mathrm{w}} + \theta \rho_{\mathrm{i}}} S_{\mathrm{T}} \frac{\partial T}{\partial t} \delta p \mathrm{d}\Omega + \int_\Omega \nabla \delta p \cdot \frac{k_{\mathrm{r}}}{\gamma^{\mathrm{w}}} \boldsymbol{k} \cdot \nabla p^{\mathrm{w}} \mathrm{d}\Omega \\ &- \int_\Omega \nabla \delta p \cdot \frac{k_{\mathrm{r}}}{\gamma^{\mathrm{w}}} \boldsymbol{k} \cdot \rho_{\mathrm{w}} \boldsymbol{b} \mathrm{d}\Omega = - \int_{\Gamma_N^{\mathrm{p}}} \bar{q}^{\mathrm{w}} \delta p \mathrm{d}\Gamma \end{aligned} \quad (47)$$

where $\bar{q}^{\mathrm{w}}$ is the water flux on the Neumann boundary Γ_{p}.

The energy balance equation, Eq. (18), is a form of an unsteady advection-diffusion equation and may require stabilization during numerical implementation. Oscillations in the temperature solution may occur in cases where heat transfer is dominated by convection and stabilization may need to be performed using various established approaches. One of the most commonly used stabilization methods is the Streamline Upwind/Petrov Galerkin (SUPG) method, first introduced by Hughes and Brooks [8]. This stabilization method is used here to choose appropriate test functions. Multiplying the energy balance equation by an arbitrary weighing function $\delta \tilde{T}$ and integrating over the domain Ω gives:

$$\int_\Omega \left[(\rho c)_{\mathrm{eff}} \frac{\mathrm{D}_{\mathrm{s}} T}{\mathrm{D}t} + \boldsymbol{a} \cdot \nabla T + L_{\mathrm{f}} \xi \frac{\mathrm{D}_{\mathrm{s}} S_{\mathrm{w}}}{\mathrm{D}t} + \nabla \cdot \boldsymbol{q} \right] \delta \tilde{T} \mathrm{d}\Omega = 0. \quad (48)$$

The weighting function in the SUPG method considering the advective term is:

$$\delta \tilde{T} = \delta T + \tau_{\mathrm{e}} \boldsymbol{a} \cdot \nabla \delta T \quad (49)$$

with

$$\tau_{\mathrm{e}} = \frac{h_{\mathrm{e}}}{2|\boldsymbol{a}|} \left(\coth \alpha - \frac{1}{\alpha} \right) \qquad \text{and} \qquad \alpha = \frac{|\boldsymbol{a}| h_{\mathrm{e}}}{2\lambda} \quad (50)$$

where h_{e} is the characteristic element length (maximum length) of the mesh and λ is the overall thermal conductivity of the porous medium. The weak form of the energy balance equation, after applying the divergence theorem, can be written as:

$$\begin{aligned} &\int_\Omega (\rho c)_{\mathrm{eff}} \frac{\partial T}{\partial t} \delta T \mathrm{d}\Omega + \int_\Omega \boldsymbol{a} \cdot \nabla T \delta T \mathrm{d}\Omega + \int_\Omega L_{\mathrm{f}} \xi S_{\mathrm{p}} \frac{\partial p^{\mathrm{w}}}{\partial t} \delta T \mathrm{d}\Omega \\ &+ \int_\Omega L_{\mathrm{f}} \xi S_{\mathrm{T}} \frac{\partial T}{\partial t} \delta T \mathrm{d}\Omega + \int_\Omega \nabla \delta T \lambda \nabla T \mathrm{d}\Omega \\ &+ \sum_e \left[\int_\Omega \tau_{\mathrm{e}} \boldsymbol{a} \cdot \nabla \delta T \left\{ (\rho c)_{\mathrm{eff}} \frac{\partial T}{\partial t} + \boldsymbol{a} \cdot \nabla T + L_{\mathrm{f}} \xi S_{\mathrm{p}} \frac{\partial p^{\mathrm{w}}}{\partial t} \right. \right. \\ &\left. \left. + L_{\mathrm{f}} \xi S_{\mathrm{T}} \frac{\partial T}{\partial t} + \nabla \cdot \lambda \nabla T \right\} \mathrm{d}\Omega \right] = - \int_{\Gamma_N^{\mathrm{T}}} \bar{q}^{\mathrm{T}} \delta T \mathrm{d}\Gamma \end{aligned} \quad (51)$$

where $\bar{q}^{\mathrm{T}}$ is the heat flux on the Neumann boundary Γ_{T}. The stabilizing term to be summed over the number of elements is not continuous in the global space.

5.3. Galerkin Formulation

The governing equations are to be solved for three field variables: displacement, pore water pressure and temperature. This forms the so called $u - p - T$ formulation. We use a mixed formulation to express the field variables in terms of the basis functions and the control point values (nodal values in FEA). Choosing the basis functions $\boldsymbol{N}_{\mathrm{u}}$,$\boldsymbol{N}_{\mathrm{p}}$ and $\boldsymbol{N}_{\mathrm{T}}$ for the displacement, pore water pressure and temperature, respectively, we write:

$$\begin{aligned} \boldsymbol{u} &= \boldsymbol{N}_{\mathrm{u}} \boldsymbol{u}^{\mathrm{c}}, & \frac{\partial \boldsymbol{u}}{\partial t} &= \boldsymbol{N}_{\mathrm{u}} \frac{\partial \boldsymbol{u}^{\mathrm{c}}}{\partial t} \\ p^{\mathrm{w}} &= \boldsymbol{N}_{\mathrm{p}} \boldsymbol{p}^{\mathrm{c}}, & \frac{\partial p^{\mathrm{w}}}{\partial t} &= \boldsymbol{N}_{\mathrm{p}} \frac{\partial \boldsymbol{p}^{\mathrm{c}}}{\partial t} \\ T &= \boldsymbol{N}_{\mathrm{T}} \boldsymbol{T}^{\mathrm{c}}, & \frac{\partial T}{\partial t} &= \boldsymbol{N}_{\mathrm{T}} \frac{\partial \boldsymbol{T}^{\mathrm{c}}}{\partial t} \end{aligned} \quad (52)$$

where $\boldsymbol{u}^{\mathrm{c}}$, $\boldsymbol{p}^{\mathrm{c}}$ and $\boldsymbol{T}^{\mathrm{c}}$ are the control point displacement, pore water pressure and temperature values. In a Galerkin formulation, we choose the arbitrary test functions to be the same as the basis functions. Application to the weak form of the equilibrium equation, Eq. (45), results in the system of equations:

$$\boldsymbol{C}_{\mathrm{uu}}\frac{\partial \boldsymbol{u}^{\mathrm{c}}}{\partial t}+\boldsymbol{C}_{\mathrm{up}}\frac{\partial \boldsymbol{p}^{\mathrm{c}}}{\partial t}+\boldsymbol{C}_{\mathrm{uT}}\frac{\partial \boldsymbol{T}^{\mathrm{c}}}{\partial t}=\boldsymbol{f}_{\mathrm{u}} \tag{53}$$

where

$$\begin{aligned}
\boldsymbol{C}_{\mathrm{uu}} &= \int_{\Omega}\nabla \boldsymbol{N}_{\mathrm{u}}^{\intercal}\boldsymbol{D}\nabla \boldsymbol{N}_{\mathrm{u}}\mathrm{d}\Omega\\
\boldsymbol{C}_{\mathrm{up}} &= \int_{\Omega}\nabla \boldsymbol{N}_{\mathrm{u}}^{\intercal}\left(\frac{\partial \boldsymbol{\sigma}}{\partial p^{\mathrm{w}}}-\boldsymbol{D}\frac{\partial \boldsymbol{\varepsilon}^{\mathrm{ph}}}{\partial p^{\mathrm{w}}}\right)\boldsymbol{N}_{\mathrm{p}}\mathrm{d}\Omega\\
\boldsymbol{C}_{\mathrm{uT}} &= \int_{\Omega}\nabla \boldsymbol{N}_{\mathrm{u}}^{\intercal}\left(\frac{\partial \boldsymbol{\sigma}}{\partial T}-\boldsymbol{D}\frac{\partial \boldsymbol{\varepsilon}^{\mathrm{ph}}}{\partial T}\right)\boldsymbol{N}_{\mathrm{T}}\mathrm{d}\Omega\\
\boldsymbol{f}_{\mathrm{u}} &= \int_{\Gamma_N^{\mathrm{u}}}\boldsymbol{N}_{\mathrm{u}}^{\intercal}\bar{\boldsymbol{t}}\mathrm{d}\Gamma.
\end{aligned}$$

Galerkin formulation to the weak form of the mass balance equation, Eq. (47), results in:

$$\boldsymbol{K}_{\mathrm{pp}}\boldsymbol{p}^{\mathrm{c}}+\boldsymbol{C}_{\mathrm{pu}}\frac{\partial \boldsymbol{u}^{\mathrm{c}}}{\partial t}+\boldsymbol{C}_{\mathrm{pp}}\frac{\partial \boldsymbol{p}^{\mathrm{c}}}{\partial t}+\boldsymbol{C}_{\mathrm{pT}}\frac{\partial \boldsymbol{T}^{\mathrm{c}}}{\partial t}=\boldsymbol{f}_{\mathrm{p}} \tag{54}$$

where

$$\begin{aligned}
\boldsymbol{K}_{\mathrm{pp}} &= \int_{\Omega}\nabla \boldsymbol{N}_{\mathrm{p}}^{\intercal}\frac{k_{\mathrm{r}}}{\gamma^{\mathrm{w}}}\boldsymbol{k}\nabla \boldsymbol{N}_{\mathrm{p}}\mathrm{d}\Omega\\
\boldsymbol{C}_{\mathrm{pu}} &= \int_{\Omega}\boldsymbol{N}_{\mathrm{p}}^{\intercal}\frac{\rho_{\mathrm{w}}S_{\mathrm{w}}+\rho_{\mathrm{i}}S_{\mathrm{i}}}{\rho_{\mathrm{w}}+\theta\rho_{\mathrm{i}}}\nabla \boldsymbol{N}_{\mathrm{u}}\mathrm{d}\Omega\\
\boldsymbol{C}_{\mathrm{pp}} &= \int_{\Omega}\boldsymbol{N}_{\mathrm{p}}^{\intercal}\frac{n(\rho_{\mathrm{w}}-\rho_{\mathrm{i}})}{\rho_{\mathrm{w}}+\theta\rho_{\mathrm{i}}}S_{\mathrm{p}}\boldsymbol{N}_{\mathrm{p}}\mathrm{d}\Omega\\
\boldsymbol{C}_{\mathrm{pT}} &= \int_{\Omega}\boldsymbol{N}_{\mathrm{p}}^{\intercal}\frac{n(\rho_{\mathrm{w}}-\rho_{\mathrm{i}})}{\rho_{\mathrm{w}}+\theta\rho_{\mathrm{i}}}S_{\mathrm{T}}\boldsymbol{N}_{\mathrm{T}}\mathrm{d}\Omega\\
\boldsymbol{f}_{\mathrm{p}} &= \int_{\Omega}\nabla \boldsymbol{N}_{\mathrm{p}}^{\intercal}\frac{k_{\mathrm{r}}}{\gamma^{\mathrm{w}}}\boldsymbol{k}\rho_{\mathrm{w}}\boldsymbol{b}\mathrm{d}\Omega-\int_{\Gamma_N^{\mathrm{p}}}\boldsymbol{N}_{\mathrm{p}}^{\intercal}\bar{q}^{\mathrm{w}}\mathrm{d}\Gamma.
\end{aligned}$$

Similarly, application to the weak form of the energy balance equation, Eq. (51), gives the system of equations:

$$(\boldsymbol{K}_{\mathrm{TT}}+\boldsymbol{K}_{\mathrm{TT}}^{\mathrm{s}})\boldsymbol{T}^{\mathrm{c}}+(\boldsymbol{C}_{\mathrm{Tp}}+\boldsymbol{C}_{\mathrm{Tp}}^{\mathrm{s}})\frac{\partial \boldsymbol{p}^{\mathrm{c}}}{\partial t}+(\boldsymbol{C}_{\mathrm{TT}}+\boldsymbol{C}_{\mathrm{TT}}^{\mathrm{s}})\frac{\partial \boldsymbol{T}^{\mathrm{c}}}{\partial t}=\boldsymbol{f}_{\mathrm{T}} \tag{55}$$

where

$$\begin{aligned}
\boldsymbol{K}_{\mathrm{TT}} &= \int_{\Omega}\nabla \boldsymbol{N}_{\mathrm{T}}^{\intercal}\boldsymbol{a}\boldsymbol{N}_{\mathrm{T}}\mathrm{d}\Omega+\int_{\Omega}\nabla \boldsymbol{N}_{\mathrm{T}}^{\intercal}\boldsymbol{\lambda}\nabla \boldsymbol{N}_{\mathrm{T}}\mathrm{d}\Omega+\int_{\Gamma_N^{\mathrm{T}}}\boldsymbol{N}_{\mathrm{T}}^{\intercal}\lambda_{\mathrm{e}}\boldsymbol{N}_{\mathrm{T}}\mathrm{d}\Gamma\\
\boldsymbol{K}_{\mathrm{TT}}^{\mathrm{s}} &= \int_{\Omega}\nabla \boldsymbol{N}_{\mathrm{T}}^{\intercal}\tau_{\mathrm{e}}\boldsymbol{a}\cdot\boldsymbol{a}\nabla \boldsymbol{N}_{\mathrm{T}}\mathrm{d}\Omega+\int_{\Omega}\nabla \boldsymbol{N}_{\mathrm{T}}^{\intercal}\tau_{\mathrm{e}}\boldsymbol{a}\cdot\boldsymbol{\lambda}\nabla(\nabla \boldsymbol{N}_{\mathrm{T}})\mathrm{d}\Omega\\
\boldsymbol{C}_{\mathrm{Tp}} &= \int_{\Omega}\boldsymbol{N}_{\mathrm{T}}^{\intercal}L_{\mathrm{f}}\xi S_{\mathrm{p}}\boldsymbol{N}_{\mathrm{p}}\mathrm{d}\Omega\\
\boldsymbol{C}_{\mathrm{Tp}}^{\mathrm{s}} &= \int_{\Omega}\boldsymbol{N}_{\mathrm{T}}^{\intercal}L_{\mathrm{f}}\xi S_{\mathrm{p}}\tau_{\mathrm{e}}\boldsymbol{a}\nabla \boldsymbol{N}_{\mathrm{p}}\mathrm{d}\Omega\\
\boldsymbol{C}_{\mathrm{TT}} &= \int_{\Omega}\boldsymbol{N}_{\mathrm{T}}^{\intercal}(\rho c)_{\mathrm{eff}}\boldsymbol{N}_{\mathrm{T}}\mathrm{d}\Omega+\int_{\Omega}\boldsymbol{N}_{\mathrm{T}}^{\intercal}L_{\mathrm{f}}\xi S_{\mathrm{T}}\boldsymbol{N}_{\mathrm{T}}\mathrm{d}\Omega\\
\boldsymbol{C}_{\mathrm{TT}}^{\mathrm{s}} &= \int_{\Omega}\nabla \boldsymbol{N}_{\mathrm{T}}^{\intercal}(\rho c)_{\mathrm{eff}}\tau_{\mathrm{e}}\boldsymbol{a}\boldsymbol{N}_{\mathrm{T}}\mathrm{d}\Omega+\int_{\Omega}\boldsymbol{N}_{\mathrm{T}}^{\intercal}L_{\mathrm{f}}\xi S_{\mathrm{T}}\tau_{\mathrm{e}}\boldsymbol{a}\nabla \boldsymbol{N}_{\mathrm{T}}\mathrm{d}\Omega\\
\boldsymbol{f}_{\mathrm{T}} &= -\int_{\Gamma_N^{\mathrm{T}}}\boldsymbol{N}_{\mathrm{T}}^{\intercal}\bar{q}^{\mathrm{T}}\mathrm{d}\Gamma+\int_{\Gamma_N^{\mathrm{T}}}\boldsymbol{N}_{\mathrm{T}}^{\intercal}\lambda_{\mathrm{e}}T_{\mathrm{e}}\mathrm{d}\Gamma
\end{aligned}$$

Letting $\boldsymbol{K}_{\mathrm{TT}}^{*}=\boldsymbol{K}_{\mathrm{TT}}+\boldsymbol{K}_{\mathrm{TT}}^{\mathrm{s}}$, $\boldsymbol{C}_{\mathrm{Tp}}^{*}=\boldsymbol{C}_{\mathrm{Tp}}+\boldsymbol{C}_{\mathrm{Tp}}^{\mathrm{s}}$ and $\boldsymbol{C}_{\mathrm{TT}}^{*}=\boldsymbol{C}_{\mathrm{TT}}+\boldsymbol{C}_{\mathrm{TT}}^{\mathrm{s}}$, the system of matrix equations, Eq. (53), (54) and (55), are summarized in to a fully coupled system as:

$$\begin{bmatrix}\boldsymbol{0} & \boldsymbol{0} & \boldsymbol{0}\\ \boldsymbol{0} & \boldsymbol{K}_{\mathrm{pp}} & \boldsymbol{0}\\ \boldsymbol{0} & \boldsymbol{0} & \boldsymbol{K}_{\mathrm{TT}}^{*}\end{bmatrix}\begin{Bmatrix}\boldsymbol{u}^{\mathrm{c}}\\ \boldsymbol{p}^{\mathrm{c}}\\ \boldsymbol{T}^{\mathrm{c}}\end{Bmatrix}+\begin{bmatrix}\boldsymbol{C}_{\mathrm{uu}} & \boldsymbol{C}_{\mathrm{up}} & \boldsymbol{C}_{\mathrm{uT}}\\ \boldsymbol{C}_{\mathrm{pu}} & \boldsymbol{C}_{\mathrm{pp}} & \boldsymbol{C}_{\mathrm{pT}}\\ \boldsymbol{0} & \boldsymbol{C}_{\mathrm{Tp}}^{*} & \boldsymbol{C}_{\mathrm{TT}}^{*}\end{bmatrix}\frac{\partial}{\partial t}\begin{Bmatrix}\boldsymbol{u}^{\mathrm{c}}\\ \boldsymbol{p}^{\mathrm{c}}\\ \boldsymbol{T}^{\mathrm{c}}\end{Bmatrix}=\begin{Bmatrix}\boldsymbol{f}_{\mathrm{u}}\\ \boldsymbol{f}_{\mathrm{p}}\\ \boldsymbol{f}_{\mathrm{T}}\end{Bmatrix} \tag{56}$$

which can be written in a more compact form as:

$$\boldsymbol{K}\boldsymbol{X}+\boldsymbol{C}\frac{\partial \boldsymbol{X}}{\partial t}=\boldsymbol{F} \tag{57}$$

where the coefficient matrices $\boldsymbol{K}$ and $\boldsymbol{C}$, the external load vector $\boldsymbol{F}$ and the vector of unknowns $\boldsymbol{X}$ are evident from Eq. (56). The matrices $\boldsymbol{K}$ and $\boldsymbol{C}$ are generally functions of $\boldsymbol{X}$, making the coupled system of equations highly nonlinear.

5.4. Numerical Implementation

We aim to solve the fully coupled system in Eq. (57) in a monolithic way since the equations are strongly coupled and highly nonlinear. Temporal discretization of the system of matrix equations is performed using the Generalized Trapezoidal Rule (GTR). For the rate of change of the unknown vector $\boldsymbol{X}$, we have the approximation:

$$\begin{aligned}
\left.\frac{\partial \boldsymbol{X}}{\partial t}\right|_{n+\theta} &= \frac{\boldsymbol{X}_{n+1}-\boldsymbol{X}_{n}}{\Delta t}\\
\boldsymbol{X}_{n+\theta} &= (1-\theta)\boldsymbol{X}_{n}+\theta\boldsymbol{X}_{n+1}
\end{aligned} \tag{58}$$

where θ is a time integration parameter which has limits $0 \leq \theta \leq 1$. The system of matrix equations at time $t_{n+\theta}$ is then:

$$\boldsymbol{K}\boldsymbol{X}_{n+\theta}+\boldsymbol{C}\left.\frac{\partial \boldsymbol{X}}{\partial t}\right|_{n+\theta}=\boldsymbol{F}_{n+\theta}. \tag{59}$$

Using the approximation in Eq. (58) into Eq. (59) and adopting a fully implicit time integration scheme with $\theta = 1$, we get:

$$[\Delta t\boldsymbol{K}+\boldsymbol{C}]_{n+1}\,\boldsymbol{X}_{n+1}=\boldsymbol{C}_{n+1}\boldsymbol{X}_{n}+\Delta t\boldsymbol{F}_{n+1}. \tag{60}$$

The residual at time step t_{n+1} is then:

$$\boldsymbol{R}_{n+1}=[\Delta t\boldsymbol{K}+\boldsymbol{C}]_{n+1}\,\boldsymbol{X}_{n+1}-\boldsymbol{C}_{n+1}\boldsymbol{X}_{n}-\Delta t\boldsymbol{F}_{n+1}. \tag{61}$$

After first-order Taylor series expansion of the residual, we solve for the increment of the unknown vector $\Delta\boldsymbol{X}_{n+1}^{i+1}$ using a Newton-Raphson iteration scheme:

$$\left.\frac{\partial \boldsymbol{R}}{\partial \boldsymbol{X}}\right|_{n+1}^{i}\Delta\boldsymbol{X}_{n+1}^{i+1}\cong-\boldsymbol{R}_{n+1}^{i} \tag{62}$$

where i is the iteration number and we have the Jacobian matrix in the above equation as:

$$\boldsymbol{J}=\frac{\partial \boldsymbol{R}}{\partial \boldsymbol{X}}. \tag{63}$$

The vector of unknowns at time step t_{n+1} is updated after each iteration using:

$$\boldsymbol{X}_{n+1}^{i+1}=\boldsymbol{X}_{n+1}^{i}+\Delta\boldsymbol{X}_{n+1}^{i+1}. \tag{64}$$

6. Numerical Examples

In this section, numerical examples are presented to verify and validate the proposed THM model. The first numerical example is presented to serve as a validation of the THM model by analyzing an isothermal consolidation problem. Some of the advantages of IGA are highlighted through this example. We then proceed to presenting ground freezing problems. In particular, we present a numerical example that deals with a one-dimensional freezing problem with drained and undrained boundary conditions. We then proceed to simulation of frost heave due to a chilled gas pipeline buried in a silty soil, where experimental observation are available for comparison with simulated results.

6.1. Isothermal Consolidation

A consolidation problem in isothermal and plane strain conditions with a known analytical solution is considered. The presence of an analytical solution serves in the verification of the numerically computed results.

6.1.1. Problem Definition

The plane strain consolidation problem considered is defined by a strip load of magnitude q applied over a width of $2a$ on a frictionless half-plane; see Figure 8. This problem is studied by several authors, for example by [30].

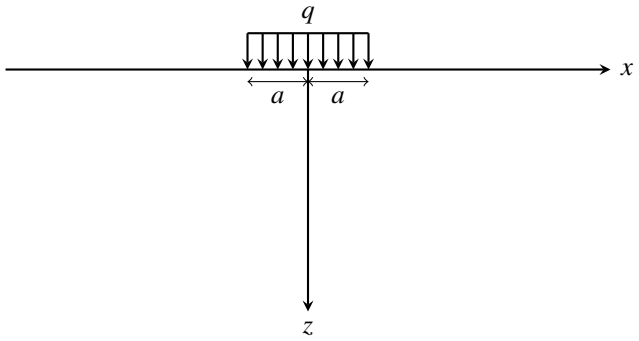

Figure 8: Isothermal consolidation: Problem definition.

The surface is assumed to be free-draining. The initial excess pore pressure for an incompressible elastic material is given by

$$p_{\mathrm{o}}^{\mathrm{w}} = \frac{q}{\pi}\left[\tan^{-1}\frac{x+a}{z} - \tan^{-1}\frac{x-a}{z}\right], \quad z > 0, \quad |x| < \infty. \tag{65}$$

The excess pore pressure at any time t, for a free-draining surface is given by

$$p^{\mathrm{w}}(t) = p_{\mathrm{o}}^{\mathrm{w}} - \frac{q}{\pi}\int_{w_1}^{w_2} \frac{1}{1+\xi^2}\exp\left[-v^2(1+\xi^2)\right]\mathrm{d}\xi \tag{66}$$

where

$$v = \frac{z}{2\sqrt{c_{\mathrm{v}}t}}, \quad w_1 = \frac{x-a}{z} \quad \text{and} \quad w_2 = \frac{x+a}{z} \tag{67}$$

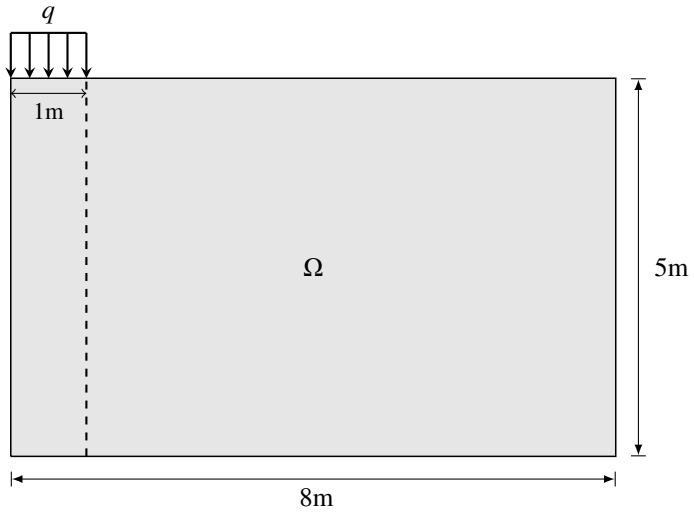

Figure 9: Isothermal consolidation: Numerical model setup.

In (67), c_{v} is the coefficient of consolidation which is expressed as

$$c_{\mathrm{v}} = \frac{2G\eta\kappa}{\gamma^{\mathrm{w}}} \tag{68}$$

in which G is the shear modulus, κ is the coefficient of permeability and, as defined in [30], η is a dimensionless parameter given by

$$\eta = \frac{1-\nu}{1-2\nu} \tag{69}$$

We study a plane strain consolidation problem with computational domain and material parameters presented in [11]. Taking advantage of symmetry, a rectangular domain with a width and height of 5 m and 8 m, respectively, is considered; see Figure 9. A strip loading of $q = 1000$ Pa is applied over a width of $a = 1$ m at the top of the left boundary. The lateral and bottom boundaries are considered as no-flux boundaries and the top boundary is assumed to be free draining. The bottom boundary is fixed in both the horizontal and vertical directions whereas the lateral boundaries are constrained in the horizontal direction. The following material parameters are used for simulation: Young's modulus $E = 3 \times 10^4$ Pa, Poisson's ratio $\nu = 0.4$, hydraulic conductivity coefficient $k = 9.81 \times 10^{-4}$ m/s and initial porosity $n = 0.5$. Both the solid and water phases are assumed to be incompressible.

6.1.2. Results

Numerical simulations are performed for varying polynomial degrees in a mixed isogeometric analysis setting. One of the advantages of IGA in comparison with traditional FEA is the ease with which higher-order simulations can be performed. We consider linear, quadratic, cubic and quartic spline basis functions ($p_{\mathrm{p}} = 1, 2, 3$ and 4) for the pressure field variable, which correspond to $p_{\mathrm{u}} = 2, 3, 4$ and 5 for the displacement field variable in a mixed formulation. The simulation domain is discretized in a graded manner such that we get a coarse mesh with 4×4 knot spans for all polynomial degrees considered.

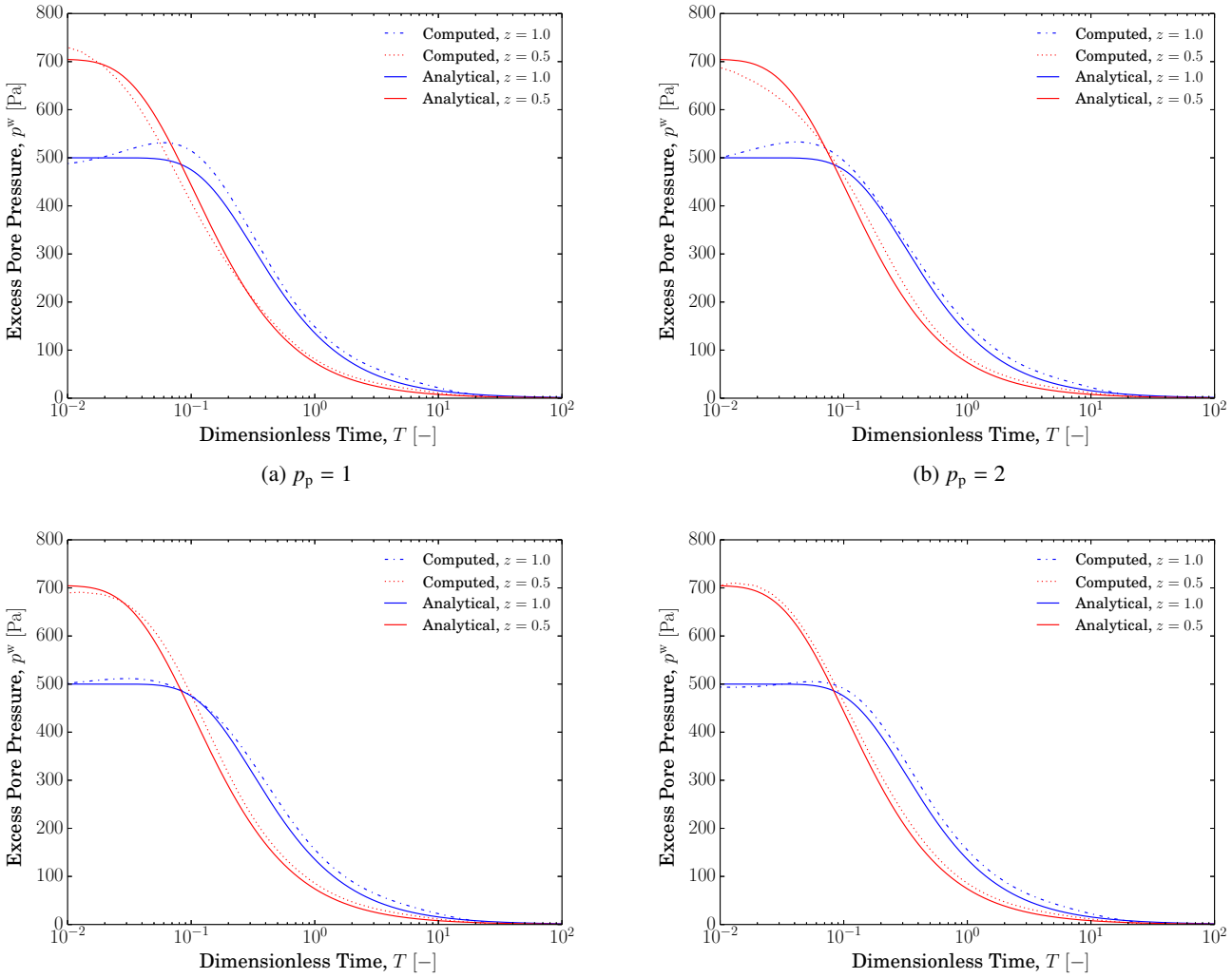

(a) $p_p = 1$ (b) $p_p = 2$

(c) $p_p = 3$ (d) $p_p = 4$

Figure 10: Isothermal consolidation: Evolution of excess pore pressure with time at $x = 0$ and selected z locations in the domain.

The evolution of the excess pore pressure versus dimensionless time T is shown in Figure 10 for selected points in the domain. The dimensionless time is given by

$$T = \frac{c_v t}{a^2} \tag{70}$$

where t is the actual time. We observe from the figure that more accurate results are obtained for higher polynomial degrees for the same levels of refinement considered. It was mentioned earlier that the k-refinement capability of IGA helps to achieve higher continuity meshes with the least number of degrees of freedom. Note that linear spline basis functions are similar with their traditional finite element counterparts. It should be noted here that, for the same number of knot spans, higher polynomial degrees result in more control points than lower polynomial degrees.

6.2. *One-dimensional Freezing*

The first numerical example we consider is the freezing of a soil column in a one-dimensional condition. This problem is studied in studied in [12] with slightly different boundary conditions.

6.2.1. *Problem Definition*

The simulation domain is a 2m long soil column with an initial homogeneous temperature of $T_o = 1\,^\circ\text{C}$, shown in Figure 11.

The soil column is subjected to cooling at the top boundary where the environment temperature is $T_e = -10\,^\circ\text{C}$. An initial hydrostatic condition is assumed for the pore water pressure throughout the soil column. The thermal conductivity of the external environment is assumed to be $\lambda_e = 0.01$ kW/m^2/K, which simulates air and other surface covering material such as snow. The freezing process is assumed to obey Newton's law of cooling such that the heat transferred in to the soil column is

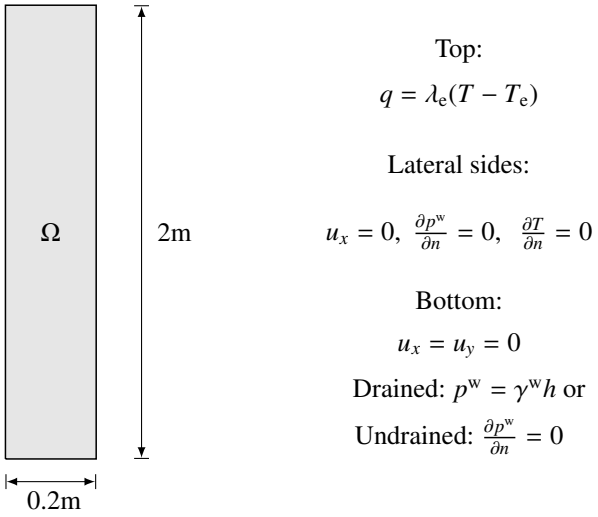

Figure 11: One-dimensional freezing: Computational domain and boundary conditions.

Table 1: One-dimensional freezing: Material and model parameters.

Parameter	**Value**	**Unit**
Thermal properties:		
Thermal conductivity of soil, λ_s	1.5	W/m/K
Thermal conductivity of water, λ_w	0.6	W/m/K
Thermal conductivity of ice, λ_i	2.2	W/m/K
Specific heat capacity of soil, c_s	800	J/kg/K
Specific heat capacity of water, c_w	4190	J/kg/K
Specific heat capacity of ice, c_i	2095	J/kg/K
Latent heat of fusion, L_f	334	kJ/kg
Hydraulic properties:		
Hydraulic conductivity, k	$1.0 \times 10^{-8(9)}$	m/s
Saturation model parameter 1, α	0.1	MPa^{-1}
Saturation model parameter 2, β	2.5	–
Saturation model parameter 3, γ	8.0	–
Hydraulic conductivity model parameter, m	0.87	–
Mechanical properties:		
Young's modulus of soil, E_s	3.0	MPa
Young's modulus of ice, E_i	9100	MPa
Poisson's ratio of soil, ν_s	0.2	–
Poisson's ratio of ice, ν_i	0.4	–
Strength model parameter, η	1.0	–
Mass and volume properties:		
Initial porosity, n	0.44	–
Density of soil, ρ_s	2650	$\mathrm{kg/m}^3$
Density of water, ρ_w	1000	$\mathrm{kg/m}^3$
Density of ice, ρ_i	910	$\mathrm{kg/m}^3$

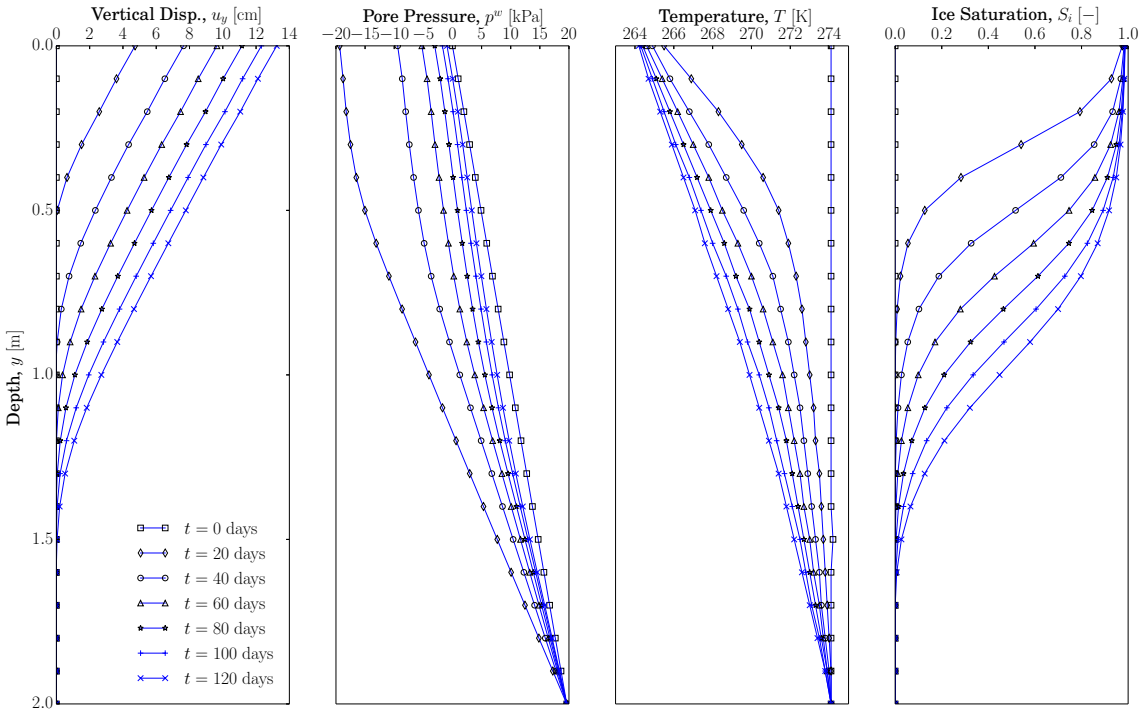

Figure 12: One-dimensional freezing: Results for a drained bottom boundary.

$q = \lambda_e(T - T_e)$. The vertical and horizontal displacements are fixed at the bottom boundary and the horizontal displacements are fixed at the lateral boundaries. The top and lateral boundaries are allowed to move freely in the vertical direction. The lateral boundaries are sealed and insulated i.e. the water and the heat fluxes are set to zero. The top boundary is assumed to be impermeable is allowed to transfer heat from the environment into the soil column, acting as a convective boundary. Two drainage boundary conditions are considered at the bottom: drained ($p^w = 0$) and undrained ($\frac{\partial p^w}{\partial n} = 0$). The material and model parameters used for the simulation are given in Table 1.

6.2.2. *Results*

Results of the simulation for a drained bottom boundary are shown in Figure 12 in terms of vertical displacement, pore water pressure, temperature and ice saturation profiles versus depth at selected time steps. The corresponding results for an undrained bottom boundary are shown in Figure 13. A comparison of the drained and undrained results shows that the temperature and ice saturation profiles of the two cases are more or less the same. This indicates that advective heat transfer has little effect on the thermal state in this particular example. On the other hand, significant differences are observed in the vertical displacement and pore water pressure profiles for the two bottom drainage cases. The final vertical heave in the drained case is larger than the heave in the undrained case by a significant margin. In the undrained case, contraction is observed as water is sucked to the freezing front. The evolution of the total vertical heave with time, at the top boundary, for the two cases is shown in Figure 14. The magnitude of permeability is known to have a significant effect in simulated heave values, for example as reported in Nishimura *et al.* (2009). This is illustrated for two different permeabilities. For decreasing values of permeability, simulations with a drained bottom boundary behave much like an undrained system.

6.3. *Frost Heave*

Prediction of frost heave is important in the design and safety analysis of structures in or on frost susceptible soils. Frost heave can cause structural damages such as displacement of retaining walls, lifting of pavements and lifting of foundations and distortion of unheated buildings, [18]. An accurate prediction and modeling of the thermal properties of such soils under sub-zero temperatures is essential. We here present a numerical example based on field-scale experimental observations on the nature of frost heaving; see Smith and Patterson [33]. The field scale test performed considers a chilled pipeline buried in soil and an outer environment with sub-zero temperature. The heave displacements from the test are documented and the results are used for comparison against simulations. Other relevant information is referred from the numerical studies by Selvadurai *et al.* [32] and Mikkola and Hartikainen [17].

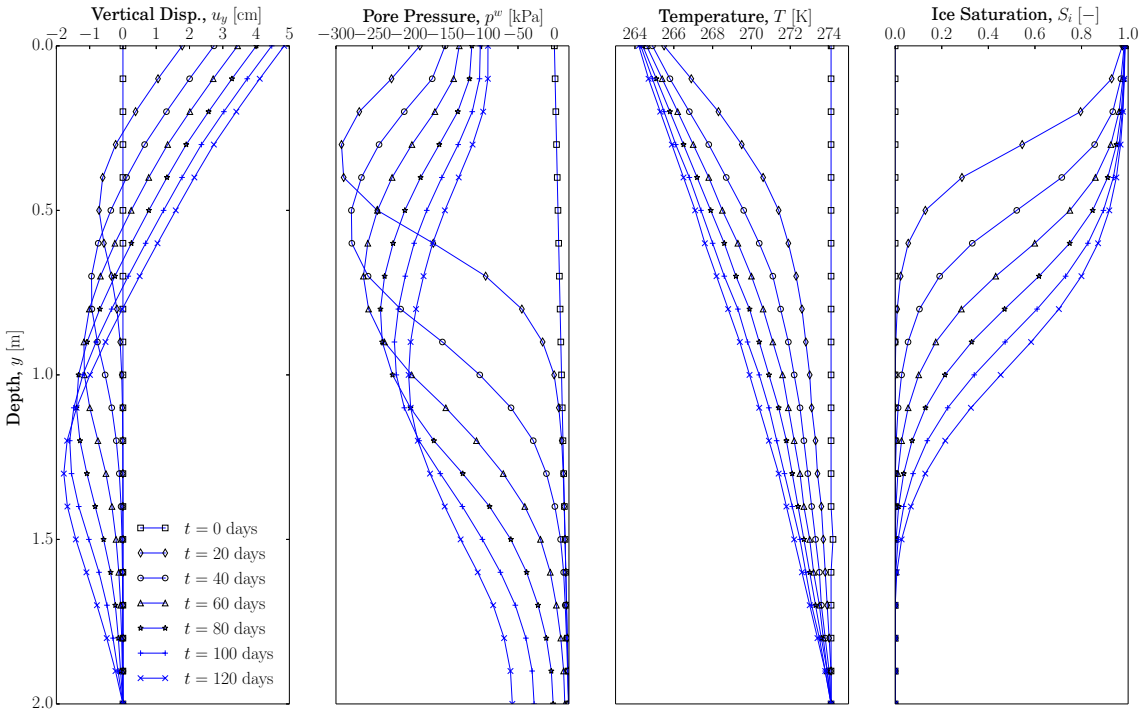

Figure 13: One-dimensional freezing: Results for an undrained bottom boundary.

6.3.1. Problem Definition

The gas pipeline in the full-scale experiment has a diameter of 273 mm and is buried in silt. The length of the pipeline is 16 m and the 8 m wide test trench is filled with silt up to a depth of 1.75 m. The backfill on top of the pipeline has a height of 0.33 m. The numerical model is setup in two dimensions and we take advantage of symmetry and model only half of the cross-sectional domain. The computational domain is shown in Figure 15. The water table is located at 90 cm below the top surface but the whole domain is assumed to be saturated due to capillarity.

The following boundary conditions are defined: both the horizontal and vertical displacements are fixed at the bottom boundary and the lateral boundaries are constrained from horizontal displacement. The bottom boundary is drained and adiabatic. The top boundary is undrained and its temperature is −0.75 °C from the hall temperature. The lateral boundaries are impermeable and adiabatic. The temperature in the pipeline is maintained at a constant value of −5 °C throughout the experiment. The initial temperature of the silt is 4 °C.

The material properties for the silt are given in Table 2. The saturation model parameters are estimated based on curve fitting to experimental data of unfrozen water content versus temperature. The hydraulic conductivity model parameter is similarly estimated by fitting a curve to an experimental hydraulic conductivity versus temperature data. The experimental data and the fitted curves are shown in Figure 16. The strength parameter is selected such that the frozen strength of the silt is comparable to empirical estimates such as in [1].

6.3.2. Results

The mesh used for the simulation is shown in Figure 17. Quadratic polynomial degrees are used for the pressure and the temperature ($p_\mathrm{p} = p_\mathrm{T} = 2$) and cubic polynomial degree for the displacement ($p_\mathrm{u} = 3$). The simulation is run for a time period of 358 days, as in the experiment.

The degree of ice saturation in the simulation domain after 358 days is shown in Figure 18. We observe from the result that freezing is initiated from two fronts; the subzero temperatures in the pipeline and the top boundary. Frost penetration occurs slowly and we see that we still have an unfrozen area in the domain after 358 days. This is due to the hydraulic and thermal properties of the silt in the experiment. Some unfrozen water still remains in areas of the frozen part, as expected from the unfrozen water content data from experiments.

The temperature profiles showing the evolution of the freezing front are presented in Figure 19 for time periods after 150, 250 and 358 days, the final step. At the end of the simulation, and the experiment, some portion of the silt still has a temperature above the freezing temperature. The evolution of the 0 °C isotherm from the simulation shows a good agreement with the experimental results reported by Smith and Patterson [33]. A total heave of about 20 cm is observed at the centerline of the

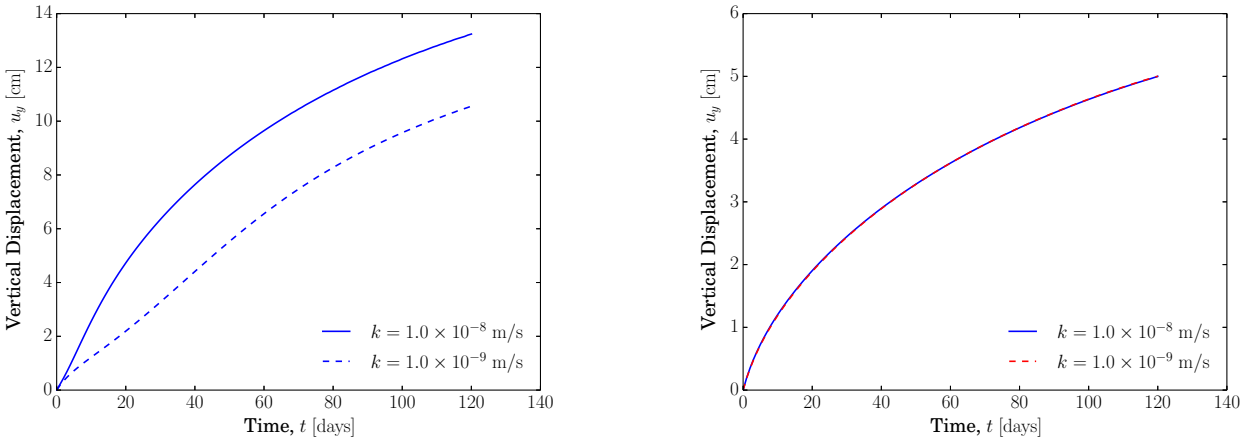

(a) Drained bottom

(b) Undrained bottom

Figure 14: One-dimensional freezing: Vertical displacement of the top boundary for different bottom drainage conditions and hydraulic conductivities.

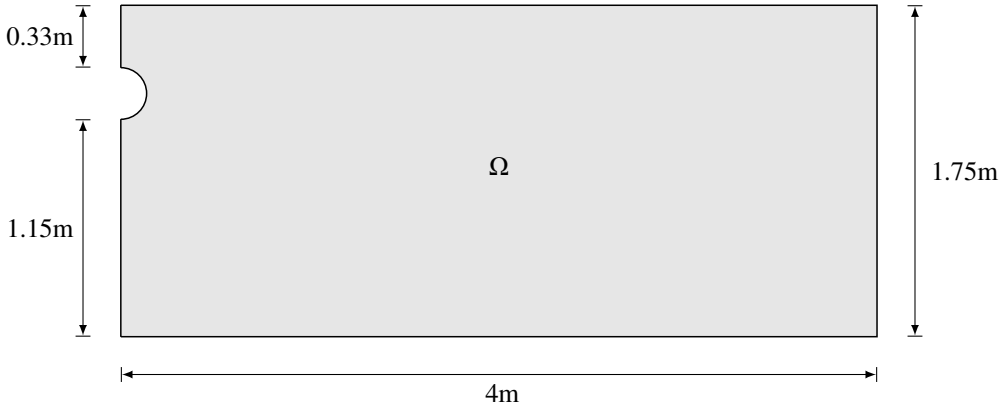

Figure 15: Frost heave: Computational domain.

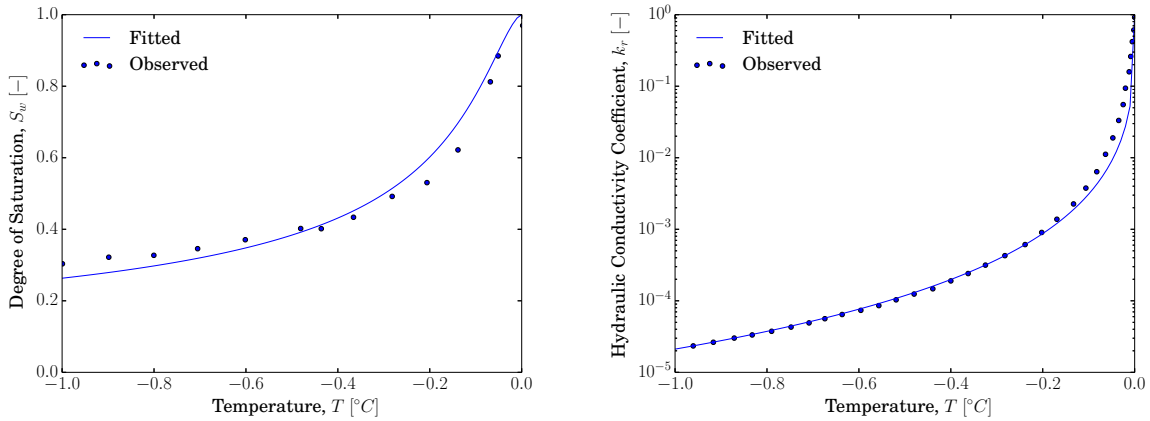

Figure 16: Frost heave: Estimation of saturation model parameters and hydraulic conductivity model parameter based on experimental data.

Table 2: Frost heave: Material and model parameters.

Parameter	**Value**	**Unit**
Thermal properties:		
Thermal conductivity of soil, λ_s	0.65	W/m/K
Thermal conductivity of water, λ_w	0.6	W/m/K
Thermal conductivity of ice, λ_i	2.2	W/m/K
Specific heat capacity of soil, c_s	800	J/kg/K
Specific heat capacity of water, c_w	4190	J/kg/K
Specific heat capacity of ice, c_i	2095	J/kg/K
Latent heat of fusion, L_f	334	kJ/kg
Hydraulic properties:		
Hydraulic conductivity, k	5.0×10^{-9}	m/s
Saturation model parameter 1, α	0.9	MPa^{-1}
Saturation model parameter 2, β	1.59	–
Saturation model parameter 3, γ	0.37	–
Hydraulic conductivity model parameter, m	0.3	–
Mechanical properties:		
Young's modulus of soil, E_s	1.0	MPa
Young's modulus of ice, E_i	9100	MPa
Poisson's ratio of soil, ν_s	0.3	–
Poisson's ratio of ice, ν_i	0.4	–
Strength model parameter, η	5.0	–
Mass and volume properties:		
Initial porosity, n	0.4	–
Density of soil, ρ_s	2650	kg/m^3
Density of water, ρ_w	1000	kg/m^3
Density of ice, ρ_i	910	kg/m^3

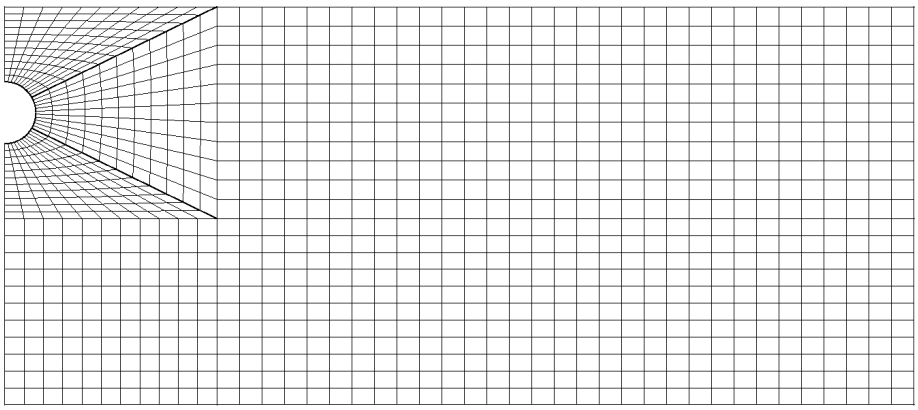

Figure 17: Frost heave: Spatial discretization.

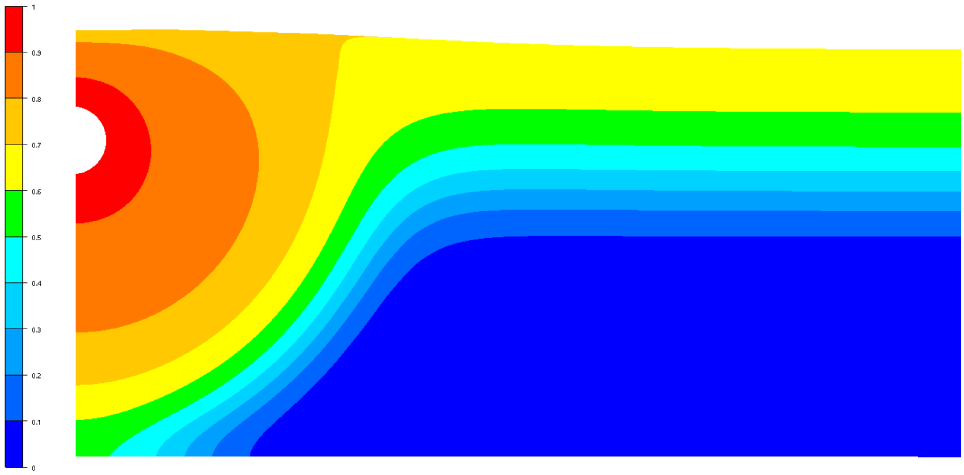

Figure 18: Frost heave: Ice saturation at the final step i.e. after 358 days.

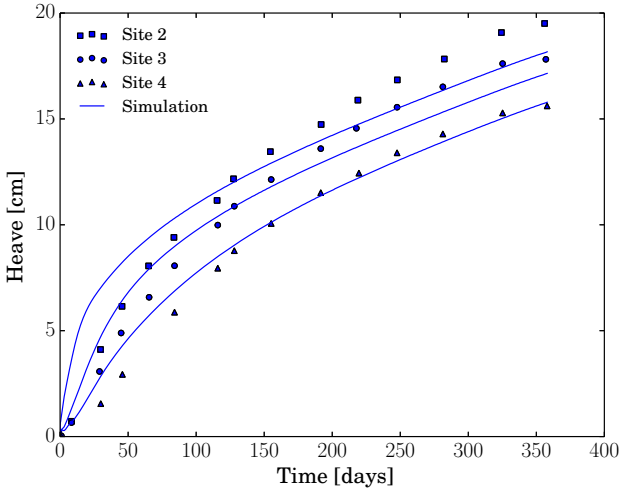

Figure 20: Frost heave: Heave displacements from experiment and simulation. The solid lines for simulation from top to bottom correspond to Site 2, Site 3 and Site 4, respectively.

pipe. The heave displacement was monitored in the experiment at locations denoted Site 2, Site 3 and Site 4, which are located at the top and 25 cm, 65 cm and 100 cm from the centerline of the pipe, respectively. The heave displacements from the simulation at these locations are plotted against the observed data and the results are shown in Figure 20. As can be seen, the results from the simulation show a reasonably good agreement with the observed data.

7. Conclusions

An isogeometric analysis based fully coupled thermo-hydro-mechanical (THM) numerical model for ground freezing is presented. The following are the main highlights of the paper:

- *THM Model*: The governing equation in the theoretical formulation of the THM coupled finite element model are derived based on porous media theory, where a saturated frozen soil with solid, water and ice phases is assumed. Volume expansion and contraction strains, due to phase change from water to ice and ice to water, are incorporated into the governing equations. The governing equations are supplemented by other equations such as the soil-water characteristic curve, slightly modified based on an existing and well known model, and the hydraulic conductivity model, adopted from literature.

- *IGA in Geomechanics*: The numerical implementation of the model is based on isogeometric analysis using B-Splines for numerical integration. The continuity of the B-Splines basis functions across knot spans, analogous to elements in the standard finite element method, can be controlled to a desired degree. This is unlike in the finite element method, where the basis function are only C^0 continuous across element boundaries. This improves the accuracy of derived quantities such as stresses, strains and fluxes. The use of isogeometric analysis also has the advantage that CAD geometries can be represented in an 'exact' manner, which are only approximated through mesh generation in the traditional finite element method. The other advantage of IGA in comparison with traditional FEA is that higher-order simulations, with high continuity and high regularity meshes, can be performed easily.

- *Numerical Studies*: An isothermal consolidation problem with an analytical solution is first studied to validate the THM model and to show some of the advantages of IGA. It is shown that higher-order IGA simulations can result in more accurate results for a given level of refinement. The model is then used to simulate freezing problems. In particular, numerical examples on one-dimensional freezing of a soil column and a two-dimensional frost heave simulation, with a pipeline transporting chilled gas, are presented. The two-dimensional frost heave problem is based on field-scale experimental data and the numerical simula-

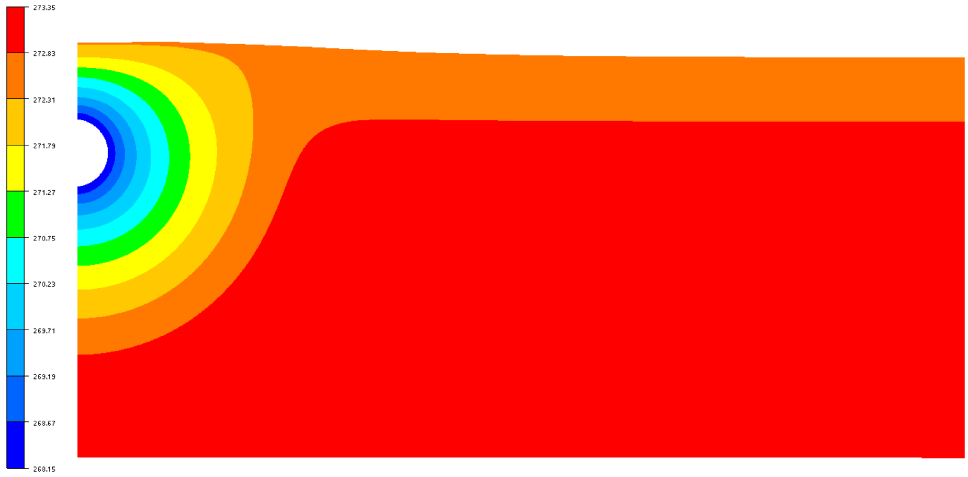

(a) t = 150 days

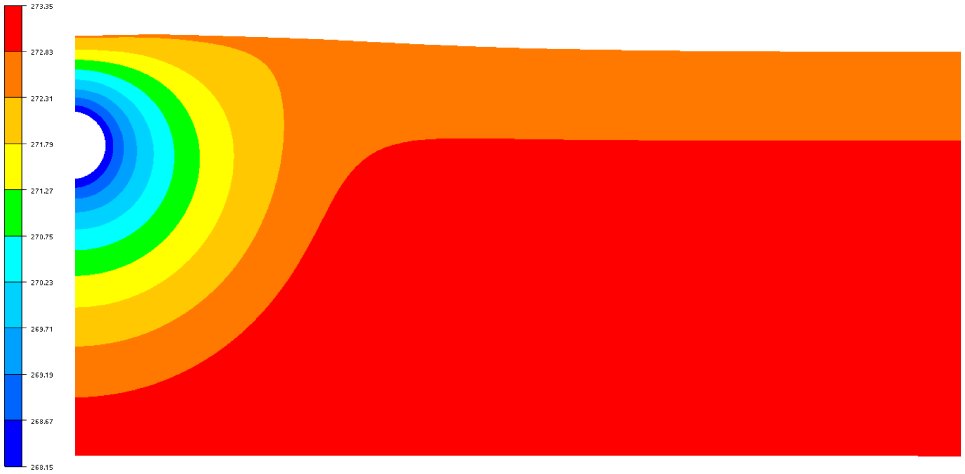

(b) t = 250 days

(c) t = 358 days

Figure 19: Frost heave: Temperature profiles at selected time steps.

tion results were observed to be in a reasonable agreement with the experimental results.

The presented THM model improved in various ways. Improving the existing soil-water characteristic curve, to consider effects such as hysteresis, is one example. It is observed from the numerical studies that the computed solutions in ground freezing are sensitive to the saturation model parameters and the hydraulic conductivity model parameter. In the current THM model, a simple nonlinear thermoelastic material model with temperature dependent parameters is incorporated. The use of advanced material models, such as elastoplastic and viscoplastic models, will improve the model further. This may help to capture some physical phenomena such as pressure melting and creep deformation of frozen soil.

Acknowledgement

This work is financially supported by the Research Council of Norway and industrial partners through the research project SAMCoT, Sustainable Arctic Marine and Coastal Technology. The authors gratefully acknowledge the support.

Appendix A. Validation of THM Model

The governing equations and the final discretized system of equations can be validated qualitatively for a specific case. The approach used here is to check if the system of equations reduce to the well-know equations of poroelasticity when no freezing is considered. This means that we assume the degree of ice saturation to be zero, i.e. $S_\mathrm{i} = 0$, which for a saturated porous medium implies $S_\mathrm{w} = 1$. A constant degree of water saturation further implies that the isothermal and non-isothermal water capacities become zero i.e. $S_\mathrm{p} = S_\mathrm{T} = 0$. With these conditions, the governing equations in Eq. (9), (12) and (18) reduce to:

$$\nabla \cdot \boldsymbol{\sigma}' - \nabla p^\mathrm{w} + \rho \boldsymbol{b} = 0 \tag{A.1}$$

$$\nabla \cdot \boldsymbol{v}^\mathrm{s} + \nabla \cdot \boldsymbol{w} = 0 \tag{A.2}$$

$$(\rho c)_\mathrm{eff} \frac{\partial T}{\partial t} + \boldsymbol{a} \cdot \nabla T = -\nabla \cdot \boldsymbol{q} + Q \tag{A.3}$$

If we further assume isothermal conditions such that there are no spatial and temporal changes in temperature i.e. $\nabla T = 0$ and $\frac{\partial T}{\partial t} = 0$, the equations effectively reduce to the governing equations of a consolidation problem with incompressible solid grains and water. The THM numerical implementation is verified by simulating a consolidation problem. The thermal material properties are supplied in the input such that the coefficient matrices related to temperature are non-zero. A positive initial temperature is assumed and all the boundaries of the consolidation model are set to be adiabatic. The results are not included here.

References

[1] O. B. Andersland and B. Ladanyi. *Frozen ground engineering*. John Wiley & Sons, 2004.

[2] J. Cote and J. M. Konrad. A generalized thermal conductivity model for soils and construction materials. *Canadian Geotechnical Journal*, 42(2):443–458, 2005.

[3] J. A. Cottrell, T. J. R. Hughes, and Y. Bazilevs. *Isogeometric Analysis : Toward Integration of CAD and FEA*. Wiley, Chichester, West Sussex, U.K., Hoboken, NJ, 2009.

[4] O. Coussy. Poromechanics of freezing materials. *Journal of the Mechanics and Physics of Solids*, 53(8):1689–1718, 2005.

[5] M. Dall'Amico, S. Endrizzi, S. Gruber, and R. Rigon. A robust and energy-conserving model of freezing variably-saturated soil. *The Cryosphere*, 5(2):469–484, 2011.

[6] K. Hansson, J. Simunek, M. Mizoguchi, L.-C. Lundin, and M. T. Van Genuchten. Water flow and heat transport in frozen soil. *Vadose Zone Journal*, 3(2):693–704, 2004.

[7] J. A. Hudson, O. Stephansson, and J. Andersson. Guidance on numerical modelling of thermo-hydro-mechanical coupled processes for performance assessment of radioactive waste repositories. *International Journal of Rock Mechanics and Mining Sciences*, 42(5):850–870, 2005.

[8] T. J. Hughes and A. Brooks. A multidimensional upwind scheme with no crosswind diffusion. *Finite element methods for convection dominated flows*, 34:19–35, 1979.

[9] T. J. R. Hughes, J. A. Cottrell, and Y. Bazilevs. Isogeometric analysis: CAD, finite elements, NURBS, exact geometry and mesh refinement. *Computer Methods in Applied Mechanics and Engineering*, 194(3941):4135–4195, 2005.

[10] Y. Kang, Q. Liu, and S. Huang. A fully coupled thermo-hydro-mechanical model for rock mass under freezing/thawing condition. *Cold Regions Science and Technology*, 95:19–26, 2013.

[11] O. Kolditz and H. Shao. Opengeosys developer-benchmark-book (ogs-dbb 5.04), 2010.

[12] H. Kyokawa and Y. W. Bekele. Numerical simulation of thermo-hydro-mechanically coupled processes during ground freezing and thawing. *Computer Methods and Recent Advances in Geomechanics*, pages 379–384, 2014.

[13] N. Li, B. Chen, F. X. Chen, and X. Z. Xu. The coupled heat-moisture-mechanic model of the frozen soil. *Cold Regions Science and Technology*, 31(3):199–205, 2000.

[14] Z. Liu and X. Yu. Coupled thermo-hydro-mechanical model for porous materials under frost action: theory and implementation. *Acta Geotechnica*, 6(2):51–65, 2011.

[15] J. P. G. Loch. Thermodynamic-equilibrium between ice and water in porous-media. *Soil Science*, 126(2):77–80, 1978.

[16] R. L. Michalowski and M. Zhu. Frost heave modelling using porosity rate function. *International Journal for Numerical and Analytical Methods in Geomechanics*, 30(8):703–722, 2006.

[17] M. Mikkola and J. Hartikainen. Mathematical model of soil freezing and its numerical implementation. *International Journal for Numerical Methods in Engineering*, 52(5-6):543–557, 2001.

[18] R. D. Miller. Freezing phenomena in soils. *Applications of Soil Physics (Hillel, D.)*, pages 254–298, 1980.

[19] S. Mu and B. Ladanyi. Modeling of coupled heat, moisture and stress-field in freezing soil. *Cold Regions Science and Technology*, 14(3):237–246, 1987.

[20] K. M. Neaupane and T. Yamabe. A fully coupled thermo-hydro-mechanical nonlinear model for a frozen medium. *Computers and Geotechnics*, 28(8):613–637, 2001.

[21] K. M. Neaupane, T. Yamabe, and R. Yoshinaka. Simulation of a fully coupled thermo-hydro-mechanical system in freezing and thawing rock. *International Journal of Rock Mechanics and Mining Sciences*, 36(5):563–580, 1999.

[22] G. P. Newman and G. W. Wilson. Heat and mass transfer in unsaturated soils during freezing. *Canadian Geotechnical Journal*, 34(1):63–70, 1997.

[23] S. Nishimura, A. Gens, S. Olivella, and R. J. Jardine. THM-coupled finite element analysis of frozen soil: formulation and application. *Geotechnique*, 59(3):159–171, 2009.

[24] T. Nowak, H. Kunz, D. Dixon, W. Wang, U.-J. Görke, and O. Kolditz. Coupled 3-D thermo-hydro-mechanical analysis of geotechnological in

situ tests. *International Journal of Rock Mechanics and Mining Sciences*, 48(1):1–15, 2011.

[25] X. M. Peng, X. B. Chen, and Y. Q. Wang. A model coupled heat, moisture and stress-field of saturated soil during freezing. *Ground Freezing 91, Vol 1*, 1:77–82, 1991.

[26] J. Qi, X. Yao, and F. Yu. Consolidation of thawing permafrost considering phase change. *KSCE Journal of Civil Engineering*, 17(6):1293–1301, 2013.

[27] J. Rutqvist, L. Börgesson, M. Chijimatsu, A. Kobayashi, L. Jing, T. Nguyen, J. Noorishad, and C.-F. Tsang. Thermohydromechanics of partially saturated geological media: governing equations and formulation of four finite element models. *International Journal of Rock Mechanics and Mining Sciences*, 38(1):105–127, 2001.

[28] J. Rutqvist, L. Börgesson, M. Chijimatsu, T. Nguyen, L. Jing, J. Noorishad, and C.-F. Tsang. Coupled thermo-hydro-mechanical analysis of a heater test in fractured rock and bentonite at Kamaishi Minecomparison of field results to predictions of four finite element codes. *International Journal of Rock Mechanics and Mining Sciences*, 38(1):129–142, 2001.

[29] L. Sanavia, B. François, R. Bortolotto, L. Luison, and L. Laloui. Finite element modelling of thermo-elasto-plastic water saturated porous materials. *Journal of Theoretical and Applied Mechanics*, 38(1-2):7–34, 2008.

[30] R. L. Schiffman, A. Chen, and J. C. Jordan. An analysis of consolidation theories. *Journal of Soil Mechanics & Foundations Div*, 1969.

[31] A. Selvadurai, J. Hu, and I. Konuk. Computational modelling of frost heave induced soil–pipeline interaction: I. modelling of frost heave. *Cold Regions Science and Technology*, 29(3):215–228, 1999.

[32] A. Selvadurai, J. Hu, and I. Konuk. Computational modelling of frost heave induced soil–pipeline interaction: II. modelling of experiments at the Caen test facility. *Cold Regions Science and Technology*, 29(3):229–257, 1999.

[33] M. Smith and D. Patterson. Detailed observations on the nature of frost heaving at a field scale. *Canadian Geotechnical Journal*, 26(2):306–312, 1989.

[34] H. R. Thomas, P. Cleall, Y.-C. Li, C. Harris, and M. Kern-Luetschg. Modelling of cryogenic processes in permafrost and seasonally frozen soils. *Geotechnique*, 59(3):173–184, 2009.

[35] F. Tong, L. Jing, and R. W. Zimmerman. A fully coupled thermo-hydro-mechanical model for simulating multiphase flow, deformation and heat transfer in buffer material and rock masses. *International Journal of Rock Mechanics and Mining Sciences*, 47(2):205–217, 2010.

[36] M. T. Vangenuchten. A closed-form equation for predicting the hydraulic conductivity of unsaturated soils. *Soil Science Society of America Journal*, 44(5):892–898, 1980.

[37] W. Wang and O. Kolditz. Object-oriented finite element analysis of thermo-hydro-mechanical (THM) problems in porous media. *International Journal for Numerical Methods in Engineering*, 69(1):162–201, 2007.

[38] W. Wang, G. Kosakowski, and O. Kolditz. A parallel finite element scheme for thermo-hydro-mechanical (THM) coupled problems in porous media. *Computers & Geosciences*, 35(8):1631–1641, 2009.

[39] Z. L. Wang, Q. Fu, Q. X. Jiang, and T. X. Li. Numerical simulation of water-heat coupled movements in seasonal frozen soil. *Mathematical and Computer Modelling*, 54(3-4):970–975, 2011.

[40] M. M. Zhou and G. Meschke. A three-phase thermo-hydro-mechanical finite element model for freezing soils. *International Journal for Numerical and Analytical Methods in Geomechanics*, 37(18):31733193, 2013.